International Journal of Biological Macromolecules 223 (2022) 684–701

Contents lists available at ScienceDirect

International Journal of Biological Macromolecules

journal homepage: www.elsevier.com/locate/ijbiomac

Thermal treatment of magnesium particles in polylactic acid polymer films elicits the expression of osteogenic differentiation markers and lipidome profile remodeling in human adipose stem cells

Chiara Argentati [a,1], Franco Dominici [b,1], Francesco Morena [a], Marco Rallini [b], Ilaria Tortorella [a], Ana Ferrandez-Montero [c], Roberto Maria Pellegrino [a], Begoña Ferrari [c], Carla Emiliani [a,d], Marcela Lieblich [e], Luigi Torre [b], Sabata Martino [a,d,*,2], Ilaria Armentano [f,**,2]

[a] Department of Chemistry, Biology and Biotechnology, Biochemical and Biotechnological Sciences, University of Perugia, 06122 Perugia, Italy
[b] Department of Civil and Environmental Engineering (DICA), University of Perugia, Strada di Pentima 4, 05100 Terni, Italy
[c] Instituto de Cerámica y Vidrio, CSIC, Campus de Cantoblanco, c/ Kelsen 5, 28049 Madrid, Spain
[d] CEMIN, University of Perugia, 06122 Perugia, Italy
[e] Department Physical Metallurgy, National Centre for Metallurgical Research (CENIM), CSIC, Avenida Gregorio del Amo 8, Madrid 28040, Spain
[f] Department of Economics, Engineering, Society and Business Organization (DEIM), University of Tuscia, Viterbo 01100, Italy

ARTICLE INFO

Keywords:
PLA
Osteoconductivity
Stem cells

ABSTRACT

The efficacy of polylactic acid (PLA)/Magnesium (Mg)-based materials for driving stem cells toward bone tissue engineering applications requires specific Mg surface properties to modulate the interface of stem cells with the film. Here, we have developed novel PLA/Mg-based composites and explored their osteogenic differentiation potential on human adipose stem cells (hASCs). Mg-particles/polymer interface was improved by two treatments: heating in oxidative atmosphere (TT) and surface modification with a compatibilizer (PEI). Different contents of Mg particles were dispersed in PLA and composite surface and bulk properties, protein adsorption, stem cell-PLA/Mg interactions, osteogenic markers expressions, and lipids composition profile were evaluated. Mg particles were uniformly distributed on the surface and in the bulk PLA polymer. Improved and modulated particle-polymer adhesion was observed in Mg particle-treated composites.

After 21 days in canonical growth culture conditions, hASCs on PLA/MgTT displayed the highest expression of the general osteogenic markers, RUNX2, SSP1, and BGLAP genes, Alkaline Phosphatase, type I Collagen, Osteopontin, and Calcium deposits. Moreover, by LC/MS QTOF mass-spectrophotometry lipidomic analysis, we found in PLA/MgTT-cells, for the first time, a remodeling of the lipid classes composition associated with the osteogenic differentiation. We ascribed these results to MgTT characteristics, which improve Mg availability and composite osteoinductive performance.

1. Introduction

Tissue engineering based on the combination of adult mesenchymal stem cells (MSCs) with biomaterials holds promise for bone tissue engineering applications [1–5]. Within these systems, MSCs provide the differentiated osteogenic cells and the release of trophic growth factors and biomolecules for establishing a bone regenerative environment [3,6], whereas the biomaterials provide the chemical-physical cues that stem cells sense and transduce in biochemical pathways to ensure stem cell adhesion, proliferation, morphology, and osteogenic differentiation [1–5].

Polylactic acid (PLA)/Magnesium (Mg)-based materials have

* Correspondence to: S. Martino, Department of Chemistry, Biology and Biotechnology, Biochemical and Biotechnological Sciences, University of Perugia, 06122 Perugia, Italy.
** Corresponding author.
E-mail addresses: aferrandez@icv.csic.es (A. Ferrandez-Montero), bferrari@icv.csic.es (B. Ferrari), sabata.martino@unipg.it (S. Martino), ilaria.armentano@unitus.it (I. Armentano).
[1] C. A. and F. D. did equal contribution to the work and are co-first authors.
[2] I.A. and S.M. did equal contribution to the work and are co-senior authors.

https://doi.org/10.1016/j.ijbiomac.2022.11.005
Received 27 July 2022; Received in revised form 29 October 2022; Accepted 1 November 2022
Available online 8 November 2022

emerged as polymeric composites with high biomedical potential for bone tissue repairing, as they combine the PLA properties with the osteoconductive and osseointegration properties of Magnesium (Mg) [7,8].

Mg is one of the most abundant intracellular divalent cations and one of the essential metals in the human body. It is involved in over 300 biological enzymatic reactions and plays a critical role in protein and nucleic acid production as well as in many other basic cellular functions [9,10]. In our contest, Mg is essential for bone health [11], because it stimulates the proliferation of osteoblasts [12] and is a cofactor of enzymes involved in bone matrix synthesis [13], as well as in the homeostasis of hydroxyapatite crystals (a major constituent of bone) [11]. Moreover, the effect of Mg^{2+} ions on inducing osteogenic differentiation by upregulating Runt-related transcription factor 2 (RUNX2) gene expression [14], and the presence of Mg in the PLA polymer profoundly enhances mineralization and promotes osteogenesis [15] have been shown.

Several authors have demonstrated a synergistic interaction between PLA and Mg [7]. In fact, while PLA inhibits the high rate of Mg degradation [16], Mg neutralizes the acid environment formed by PLA breakdown by-products, resulting in increased compatibility of cells generated by the release of Mg ions [8,17]. On the other hand, the interface microstructure of PLA could strongly affect the properties of the Mg-based composite films, reducing the interaction between the polymer and Mg [18].

Hence, the efficacy of the PLA/Mg composite toward biological target applications depends on the appropriate design of the polymer film, but also on the type of Mg used (*e.g.*: Mg ions, Mg particles, Mg alloys) [10,14,17,19,20] and foremost of the consequent surface composition and properties acquired by the polymer film where the metal was dispersed. In this regard, our group has demonstrated that the modification of Mg particles through a surface modifiers adsorption approach has a positive effect on the biodegradation of PLA/Mg films [20].

In this work, we explored the potential of novel Mg-based PLA composites for osteogenic differentiation of human adipose stem cells (hASCs). The composites were generated through the dispersion of Mg particles in PLA polymer by using a melt-based process and comparing two different surface modification approaches, consisting of thermal treatment and a physical encapsulation. We demonstrated that the abovementioned surface modification processes drive interfacial adhesion and dispersibility of Mg particles in the PLA polymer matrix. The best performance was obtained with thermal-treated Mg particles in PLA which trigger the expression of osteogenic markers at gene and protein levels and cause a remodeling in some lipid classes, resulting in the osteogenic differentiation of hASCs in the absence of soluble exogenous inductive molecules.

2. Materials & methods

2.1. Materials

Polylactide (PLA) grade 2003D, having a specific gravity of 1.24 $g{\cdot}cm^{-3}$ and a melting flow rate (MFR, 210 °C, 2.16 kg) of 6 g/10 min was supplied by Nature Works. Magnesium (Mg) particles were supplied by Nitroparis®. Polyethylenimine (PEI), Mv 25,000, was supplied by Sigma Aldrich, Germany.

2.2. Processing

PLA-based composite films were developed by using Mg particles at weight content selected according to our previous works [7,21]. In particular, pristine and modified Mg particles will be used. In the following section, a detailed description of the treatments used for modifying the surface property of the particles, the composite processing methods and the characterization analysis were reported.

2.2.1. Thermal treatment of Mg particles

Pristine Mg particles were thermal-treated at 350 °C in air for 1 h. To study the effect of the selected temperature, the thermal-treated Mg particles (MgTT) were analyzed by using field emission scanning electron microscopy (FESEM, Supra25Zeiss, Germany), infrared spectroscopy (FT-IR JASCO 615) in ATR mode and thermogravimetric analysis by TGA, Seiko Exstar 6300.

2.2.2. Composite granules of PLA and Mg modified by PEI masterbatch

The surfaces of the particles were modified by the adsorption of PEI dispersant in aqueous suspension and lately dispersed in a PLA solution using a colloidal mixing, under vigorous mechanical stirring and dried to obtain final composite granules, as previously reported [20]. Masterbatch with Mg particles at 30 wt% in PLA matrix was developed and used for the composite film design. The microstructure of the masterbatch granules was analyzed by scanning electron microscopy (SEM-FEG HITACHI S-4800, Japan). Thermal properties of the masterbatch were analyzed by differential scanning calorimetry (DSC- TA Q100 DSC equipment), through two different scans. The first heating (10 °C/min) determines the composite behavior and the polymer crystallinity after the PEI modification and the second heating (10 °C/min) was performed and studied once the thermal history was eliminated. As PLA studied does not crystallize from the melting state, the cooling scan was not analyzed. Materials were analyzed by comparing the glass transition, the cold crystallization and the melting temperatures. The crystallinity fraction ($\%X_c$) was calculated using the cold crystallization enthalpy (ΔH_{cc}) and the melting enthalpy (ΔH_m) from the heating curves following the Eq. (1) where ΔH_m^0 is the enthalpy of PLA with 100 % crystallinity (93.1 J/g). The crystallinity fraction was calculated taking into account the sample weight and the Mg %.

$$X_c = \frac{(\Delta H_m - \Delta H_{cc})}{w_{PLA}\Delta H_m{}^0} \quad (1)$$

Thermal degradation behavior of as-received PLA pellets and PLA/Mg-PEI composite was determined by thermal degradation analysis (TGA- model TAQ500, EEUU), over the temperature range of 20–500 °C under argon atmosphere. Fourier transform infrared spectroscopy (FT-IR) was evaluated in diffuse reflectance modality. A Nicolet Avatar 360 FTIR spectrometer was used operating in the 4000–400 cm^{-1} spectral range with a resolution of 4 cm^{-1}. For each sample about 10 mg were mixed with potassium bromide (KBr) FTIR grade, that was used also as background reference.

2.2.3. Processing of composite films

Composite films based on different content and treatment of Mg particles were processed in a twin corotating screws microextruder (Dsm Explore 5&15 CC Micro Compounder). Films 35 mm wide and with a thickness ranging between 40 and 100 μm were obtained by coupling the extruder with a DSM Film Device and using the adequate cast film die. The temperature profile was set up at 180–190–200 °C in the three extruder heating zones and a screw speed of 120 rpm was used, mixing for 3 min. Two different Mg modifications were used to produce the PLA-based composite materials: the particles subjected to a thermal treatment (MgTT) and the particles subjected to a compatibilization treatment with PEI (MgPEI) and dispersed in a masterbatch in the same PLA. The masterbatch was properly dosed and mixed with the PLA matrix to obtain the selected Mg wt% contents. Finally, the MgTT and MgPEI were dispersed at 5 wt% and 10 wt% content in the PLA by microextruder. The final material formulations are reported in Table 1. The content of Mg particles was selected according to the literature [7,21]. The results were compared to the pristine Mg particles.

2.3. Composite characterization

2.3.1. Mechanical properties

Mechanical characterization was performed at room temperature by

Table 1
Material formulations.

Material	PLA (wt%)	Mg (wt%)	MgTT (wt%)	MgPEI (wt%)
PLA	100	–	–	–
PLA/5Mg	95	5		
PLA/10Mg	90	10		
PLA/5MgTT	95	–	5	–
PLA/10MgTT	90	–	10	–
PLA/5MgPEI	95	–	–	5
PLA/10MgPEI	90	–	–	10

tensile tests method (ISO 527 Standard) with rectangular samples (100 × 10 mm^2) with a crosshead speed of 5 mm min^{-1} and a load cell of 50 N, in a digital dynamometer LR 30K Lloyd Instrument and the initial clamp gap was 50 mm. Tensile strength (σ_{max}), strain at maximum strength ($\varepsilon_{\sigma max}$), and elastic modulus (E) were calculated by the stress-strain curves.

2.3.2. Morphological analysis

Morphological characterization was performed on cryo-fractured samples by field emission scanning electron microscope (FESEM Supra 25, Zeiss, Germany). Samples were gold sputtered before the analysis.

2.3.3. Thermal properties

Thermal characterization was performed by differential scanning calorimeter (DSC) and thermogravimetric analysis (TGA). DSC tests were conducted by using a TA Instruments, Mod. Q200 from −25 °C to 200 °C at 10 °C·min^{-1} under nitrogen flow rate, with two heating and one cooling scans. The first heating scan was used to erase all thermal history. TGA was performed by using a Seiko Exstar 6300 microbalance, in a nitrogen atmosphere (250 mL·min^{-1} flow rate), from 30 °C to 600 °C at 10 °C·min^{-1}.

2.3.4. Contact angle

The surface properties of PLA-based films were evaluated by dynamic contact angle measurements, by using FTA1000 Analyser (USA) with the sessile drop method in air with HPLC-grade water. The effect of the presence Mg particles content, and surface modification on the wettability of polymeric composite films were studied by water contact angle (WCA) measurements and images.

2.3.5. FT-IR spectroscopy

Fourier transform infrared spectroscopy (FT-IR) was evaluated in diffuse reflectance modality. A Nicolet Avatar 360 FTIR spectrometer was used operating in the 4000–400 cm^{-1} spectral range with a resolution of 4 cm^{-1}. For each sample about 10 mg were mixed with potassium bromide (KBr) FTIR grade, that was used also as background reference.

2.3.6. Protein adsorption assay

For protein adsorption assessments, a series of samples, respectively of bovine serum albumin (BSA, Sigma Aldrich, St. Louis, MI, USA), at the concentration of 2 mg/mL, heat-inactivated fetal bovine serum (FBS, Euroclone, Pero (MI), Italy) at the concentration of 2 % and 10 % respectively, and plasma from normal donors at the concentration 5 mg/mL, were loaded on pristine PLA and composites films surfaces (PLA, PLA/5Mg, PLA/10Mg, PLA/5MgTT, PLA/10MgTT, PLA/5MgPEI and PLA/10MgPEI). According to our previous works, proteins were incubated at 37 °C for either 30 min or 24 h [22,23]. After three washing steps in H_2Od, the total protein content was measured by the Bradford method using the BSA, as a reference curve standard. A microtiter plate reader (ELISA Reader, GDV-DV990BV6, Roma, Italy) has been used to measure the absorption at 595 nm. Each sample was analyzed in three separate experiments, and the data reported are the mean value ± the standard error of the average of each group.

2.4. Culture of adult stem cells on PLA and composite films

2.4.1. Adipose stem cell culture

Adult adipose stem cells were used to evaluate the interaction with PLA, PLA/5Mg, PLA/5MgTT and PLA/5MgPEI composite films. Experiments were conducted by using human adipose stem cells (hASCs), already available in our laboratories [24–27]. hASCS were cultured in the growth medium, RPMI-1640 (Euroclone, Pero (MI), Italy) supplemented with 10 % of heat-inactivated FBS (Euroclone, Pero (MI), Italy), 1 % L-glutamine (Euroclone, Pero (MI), Italy), 1 % penicillin/streptomycin, seeded in tissue culture flasks (TCP) and then incubated at 37 °C, 5 % CO_2. hASCs grow as adherent fibroblast-like cells and every three days the medium was changed [22,26].

2.4.2. Film sterilization and stem cell seeding

Each film (PLA, PLA/5Mg, PLA/5MgTT and PLA/5MgPEI) was cut into squares (1 cm^2) and sterilized through immersion in 70 % ethanol for 10 s, followed by three rinses in PBS, and then deposited in 24-well plate. The stem cell suspension of 1.5 × 10^3 cells was seeded dropwise, on sterilized film and then 500 μL of culture medium was gradually added. The cultures were incubated at 37 °C in a humidified atmosphere with 5 % CO_2 and the medium was changed every three days. As an internal control, experiments were performed on stem cells seeded on glass coverslip (GC) and tissue culture polystyrene (TCP). The cell viability, morphology, and osteogenic differentiation of stem cells cultured on neat PLA and composite films were evaluated at different time points.

To assess the effect of Mg released in the culture medium, we co-cultured hASCs with each film for 21 days on trans-well plates that separate stem cells and polymer film in the same culture system. In detail, the same stem cell number (1.5 × 10^3) was seeded on a 12-well plate with 500 μL of growth culture medium, whereas sterilized (1cm^2) squares films were put into Millicell® Cell Culture Inserts (Sigma-Aldrich, St. Louis, MO, USA). The latter were placed within the 12-well plate containing stem cells previously seeded. The cultures were incubated in the growth culture medium at 37 °C in a humidified atmosphere with 5 % CO_2 for 21 days of culture and the medium was changed every three days.

2.4.3. MTT assay

Stem cell viability on neat PLA and PLA/5Mg, PLA/5MgTT and PLA/5MgPEI composite films were evaluated at different time points (3, 7, 14, 21, and 30 days) with MTT (3-(4,5-dimethylthiazol-2-yl)-2,5-diphenyltetrazolium bromide) (Sigma-Aldrich, St. Louis, MO, USA) assay, according to the manufacturer's recommendation. As an internal control, parallel experiments were conducted by seeding stem cells on TCP. The interference effects of each polymer film snippet squares on the MTT assay were also considered without stem cells. The samples' absorbance at 589 nm with a reference wavelength of 650 nm was measured using a microtiter plate reader (ELISA reader, GDV-DV990BV6, Roma, Italy).

2.4.4. Osteogenic differentiation

The osteogenic effect of Mg composite polymer films was evaluated by seeding hASCs on sterilized neat PLA and PLA/5Mg, PLA/5MgTT, and PLA/5MgPEI composite films, and culture in the growth medium. As an internal control, osteogenic differentiation of hASCs (CTR+) was achieved using hMSC differentiation basal medium supplemented with osteogenic SingleQuots™ (Lonza Walkersville, Inc., Walkersville, MD, USA): dexamethasone, L-glutamine, ascorbate, pen/strep, mesenchymal cell growth supplement (MCGS), and β-glycerophosphate. Untreated hASCs were cultured in the growth medium (CTR−). All cultures were maintained for 21 days in a humidified incubator at 37 °C and 5 % CO_2, and the culture medium was changed every three days.

2.4.5. Osteogenic differentiation assays

2.4.5.1. Alizarin red staining and quantitative analysis. The staining was performed according to previous works [24,28]. Cells on PLA, and PLA/5Mg, PLA/5MgTT, PLA/5MgPEI composite films, and on TCP (CTR+ and CTR−) at day 21 of culture were rinsed with PBS, fixed in 4 % paraformaldehyde for 20 min and after washing in H_2Od, were incubated with 500 μL of Alizarin red staining (Lonza Walkersville Inc., Walkersville, MD, USA) solution for 30 min at room temperature (RT). Cells were washed with distilled water and photos were captured with a Canon digital camera (PowerShot G10, Canon, Tokyo, Japan) and brightfield microscopy (Eclipse-TE2000-S, Nikon).

Quantitative analysis of Alizarin Red Staining was performed according to the manufacturer's instructions (Lonza Walkersville Inc., Walkersville, MD, USA) [28]. Briefly, Alizarin Red was extracted from stained cells in 400 μL 10 % acetic acid and incubated for 30 min by shaking, heated to 85 °C for 10 min, transferred to the ice for 5 min, and centrifuged at 20,000 ×*g* for 15 min. Colorimetric quantification of Alizarin Red extracted solution was measured using a microtiter plate reader (ELISA reader, GDV-DV990BV6, Roma, Italy) at 405 nm and absorbance was referred to Alizarin Red standards curve.

2.4.5.2. Alkaline phosphatase staining. For Alkaline Phosphatase (ALP) staining, cells on PLA, and PLA/5Mg, PLA/5MgTT, PLA/5MgPEI composite films, and on TCP (CTR+ and CTR−) were rinsed twice with PBS, fixed in 4 % paraformaldehyde for 20 min and after washing in H_2Od were incubated with 500 μL of FAST BCIP/NBT (Sigma-Aldrich, St. Louis, MO, USA) substrate solution for 2 h at RT. All above samples were washed twice with distilled water and photos were captured with a Canon digital camera (PowerShot G10, Canon, Tokyo, Japan) and brightfield microscopy (Eclipse-TE2000-S, Nikon).

2.4.6. Immunofluorescences

Immunofluorescences were performed as previously described [28–30]. Briefly, cells on PLA, and PLA/5Mg, PLA/5MgTT, PLA/5MgPEI composite films, and on GC (CTR+ and CTR−) were rinsed twice with PBS and fixed in 4 % paraformaldehyde for 20 min and, after PBS washing, permeabilized (PBS + FBS10%, 0.5 % Triton X-100) for 30 min at room temperature (RT) and incubated in blocking solution (PBS + FBS 10 %, 0.1 % Triton X-100) for 1 h at RT. For stem cell morphology, samples were incubated for 20 min with phalloidin (Alexa-fluor-488 phalloidin, Invitrogen, Grand Island, NY, USA) for the detection of F-actin, and overnight at 4 °C with anti-βTubulin primary antibodies (Elabscience, Houston, Texas, USA), followed by 1 h at RT with secondary antibody Donkey anti-Mouse Alexa-Fluor595-nm conjugated (Invitrogen, Grand Island, NY, USA).

To assess the osteogenic differentiation of hASCs cultured on PLA, and PLA/5Mg, PLA/5MgTT, PLA/5MgPEI composite films, samples were incubated overnight at 4 °C with the primary antibodies: antitype I Collagen (COL.1) (Chemicon International, Inc. Temecula, California, USA) and anti-Osteopontin (SPP1) (Sigma-Aldrich, St. Louis, MO, USA) followed by 1 h at RT with secondary antibody Donkey anti-Rabbit Alexa-Fluor488-nm conjugated (Invitrogen, Grand Island, NY, USA).

Finally, after being washed with PBS, all samples were mounted and nuclei were counterstained with Vectashield® with DAPI (4,6-diamidino-2-phenylindole; Vector Laboratories Inc., Burlingame, CA, USA). Immunofluorescences were evaluated by fluorescence microscope Eclipse-TE2000-S (Nikon, Tokyo, Japan) equipped with the F-View II FireWire camera (Soft Imaging System, Olympus, Germany).

2.4.7. Real-time PCR

Total RNA for gene expression analyses was purified from cells on PLA, and PLA/5Mg, PLA/5MgTT, PLA/5MgPEI composite films, and on TCP (CTR+ and CTR−) at 21 days of the culture. For gene expression analyses, total RNA was extracted by using Real Genomics Total RNA Extraction Kit YRB 100 (RBC Bioscience) according to the manufacturer's instructions. The quality and concentration of purified RNA were evaluated by the Qubit RNA HS assay Kits (molecular probes, Invitrogen, Grand Island, NY, USA), using the RNA programme. Reverse transcription was carried out using 500 ng of total RNA, converted to cDNA using PrimeScript RT Master Mix (Perfect Real Time, Takara Bio INC.). Real-time RT-PCR was performed using the different primers (Table 2), and qPCR was performed using the TB Green® Premix Ex Taq™ (Tli RNase H Plus, Takara Bio INC.) kit as directed by the manufacturer. The amplification conditions were optimized for the Step One Real-Time PCR system (Applied Biosystems) machine and assays were run in triplicate. The relative quantification of mRNA of each gene was determined by the comparative $2^{-\Delta\Delta C\tau}$ method where the target is normalized with the GAPDH gene. The data are presented as the mean ± SD of three technical replicates.

2.4.8. FESEM analysis

Stem cell–film interaction was evaluated by FESEM after 7 days of culture. Cells on PLA, PLA/5Mg, PLA/5MgTT and PLA/5MgPEI films were rinsed twice with PBS and fixed in 2.5 % glutaraldehyde for 30 min at RT then dehydrated by adding progressively more concentrated ethanol (5–100 % v/v) every 5 min and finally dried by the Critical Point machine (CPD, Emitech K850). Once dried, the samples were gold sputter coated before examination by FESEM (Supra 25 Zeiss) at an accelerating voltage of 5 kV.

2.4.9. Lipid extraction and LC/MS QTOF analysis

Lipid extraction of cells cultured on PLA, PLA/5Mg, PLA/5MgTT and PLA/5MgPEI and CTR−, CTR+, for 21 days was carried out using the method described by Pellegrino et al. with minor differences [31]. Each pellet was spiked with the same volume of freshly prepared MMC extraction mixture, prepared by mixing 1 mL of standard Splash Lipidomix (Avanti Polar) diluted 1:10 in Methanol, 1 mL of Methyl tert-butyl ether and 1 mL of Chloroform. After vortexing, the samples were placed in a T-Shaker (Euroclone, Pero (MI), Italy) and processed for 20 min at 1500 rpm and 20 °C. Afterward, the samples were then centrifuged for 10 min at 13,000*g* at 4 °C and the supernatant was transferred to an autosampler vial and dried with a gentle stream of N2. The residue was resuspended with 100 μL of a 9:1 Methanol/Toluene solution and immediately subjected to LC/MS analysis.

LC/MS analyses were carried out using the validated analytical method described by Koelmel et al. [32], adapted to the different instrumental configurations. Briefly, LC/MS QTOF analysis was performed using a 1260 Infinity II LC System coupled with an Agilent 6530 Q-TOF spectrometer (Agilent Technologies, Santa Clara CA USA). Separation was carried out on a reverse phase C18 column (Agilent InfinityLab Poroshell 120 EC-C18, 3.0 × 100 mm, 2.7 μm) at 50 °C and 0.6 mL/min flow. The mobile phase consisted of a mixture of water (A), ACN (B), MeOH (C), and IPA (D) all containing a concentration of 10 mM ammonium acetate and 0.2 mM of ammonium fluoride except for ACN. Gradient was: time 0–1 min isocratic at A 27 %, B 14 %, C 24 %, D 35 %; time from 1 to 3.5 min: linear-gradient to A 12.6 %, B 17.2 %, C 27.2 %, D 43 %; time 3.5–10 min isocratic; time from 10 to 11 min: linear-gradient to A 0 %, B 20 %, C 30 %, D 50 %; time 11–17 min isocratic; time 17–17.1 min: linear-gradient to A 27 %, B 14 %, C 24 %, D 35 %; time 19 min: stop run.

An iterative MS/MS acquisition mode on three technical replicates

Table 2
Primers used in the qRT-PCR.

Primers	Forward	Reverse
GAPDH	TTAACTCTGGTAAAGTGGATATTGT	GATCTCGCTCCTGGAAGA
RUNX2	ATCTCCGCAGGTCACTACCA	ACTGTGCTGAAGAGGCTGTTT
BGLAP	CACACTCCTCGCCCTATTG	GGTCTCTTCACTACCTCGCT
SPP1	TGAAACTGTGCCAGCCAAAC	ACCCCCAAGGCAGCTCTATT

for each sample was used. The Agilent JetStream source operated as follows: Gas Temp (N_2) 200 °C, Drying Gas 10 L/min, Nebulizer 50 psi, Sheath Gas temp: 300 °C at 12 L/min. MS/MS spectra were obtained using N_2 at 30 V CE.

Raw data were processed using MS-DIAL software (4.48) [33] to perform peak-picking, alignment, annotation, quantification, and polarity amalgamation. Lipid annotation at the molecular species level was carried out according to the recommendations of Lipid Standard Initiative [34] using MS and MS/MS acquired data. Lipids quantification was carried out using a specific deuterated internal standard for each lipid class, according to the method described by Tsugawa H. et al. [33].

2.4.10. Lipid mass data analysis

The lipidomic analysis produced a list of over 600 different lipid species, along with their relative abundances. These were first processed by grouping lipid species in classes and then transforming them into mol % of all lipids detected. The classes were: Acylcarnitine (CAR), Cardiolipin (CL), ceramide (Cer), diacylglycerol (DG), free fatty acid (FA), lyso-PC (LPC), N-acylethanolamines (NAE), phosphatidylcholine (PC), phosphatidylethanolamine (PE), phosphatidylinositol (PI), phosphatidylserine (PS), sphingomyelin (SM), triacylglycerol (TG), while all other classes with mol % less than one were grouped in a unique class (Other).

Non-deterministic and non-linear dimension reduction t-distributed stochastic neighbor embedding (tSNE) was performed to cluster data using the 'Rtsne' library embedded in R software (v.4.1.0).

2.5. Statistical analysis

Data analysis was reported as mean ± SD. A post-hoc comparison test was carried out using the one-way ANOVA and Dunn's Multiple Comparison Test (GraphPad 6.0 Software, San Diego, CA, USA). The $p < 0.05$ was considered statistically significant. Significance of the differences was indicated as follows: *p < 0.05; **$p < 0.01$; ***$p < 0.001$, **** $p < 0.0001$.

3. Results

3.1. Characterization of thermal-treated Mg particles

First, we analyzed the morphological, thermal, and chemical properties of thermal-treated Mg particles, compared to pristine ones (Fig. 1). FESEM micrograph of as-received Mg powder highlighted the presence of particles with spherical morphology with a diameter ranging to 10 μm and the presence of satellite particles (Fig. 1A). The thermal-treated Mg particles maintain the spherical shape (Fig. 1B), with an increase of surface roughness on the spherical surface, with the evidence of small cracks and porous structure on the Mg particle surface.

The infrared spectrum of Mg particles performed in reflection mode indicated the presence of a sharp peak at 3700 cm^{-1} corresponding to the O—H stretching mode of hydroxyl groups (Fig. 1C) [35]. Because this peak was observed before dehydration, we inferred that it was derived from the $Mg(OH)_2$ surface and the moisture present on the surface. After the thermal treatment at 350 °C in air for 1 h, this peak strongly decreases, as expected when the reaction of dihydroxylation occurred [36]. Infrared spectra showed a strong absorption band in the region 400–800 cm^{-1}, due to the stretching vibrations derived from Mg—O bonds [35,37], that are present in pristine and thermal-treated Mg particles. The main infrared spectra difference in Fig. 1C can be attributed to the process of $Mg(OH)_2$ dehydroxylation. In fact, the thermal treatment performed in an oxidative atmosphere was conducted

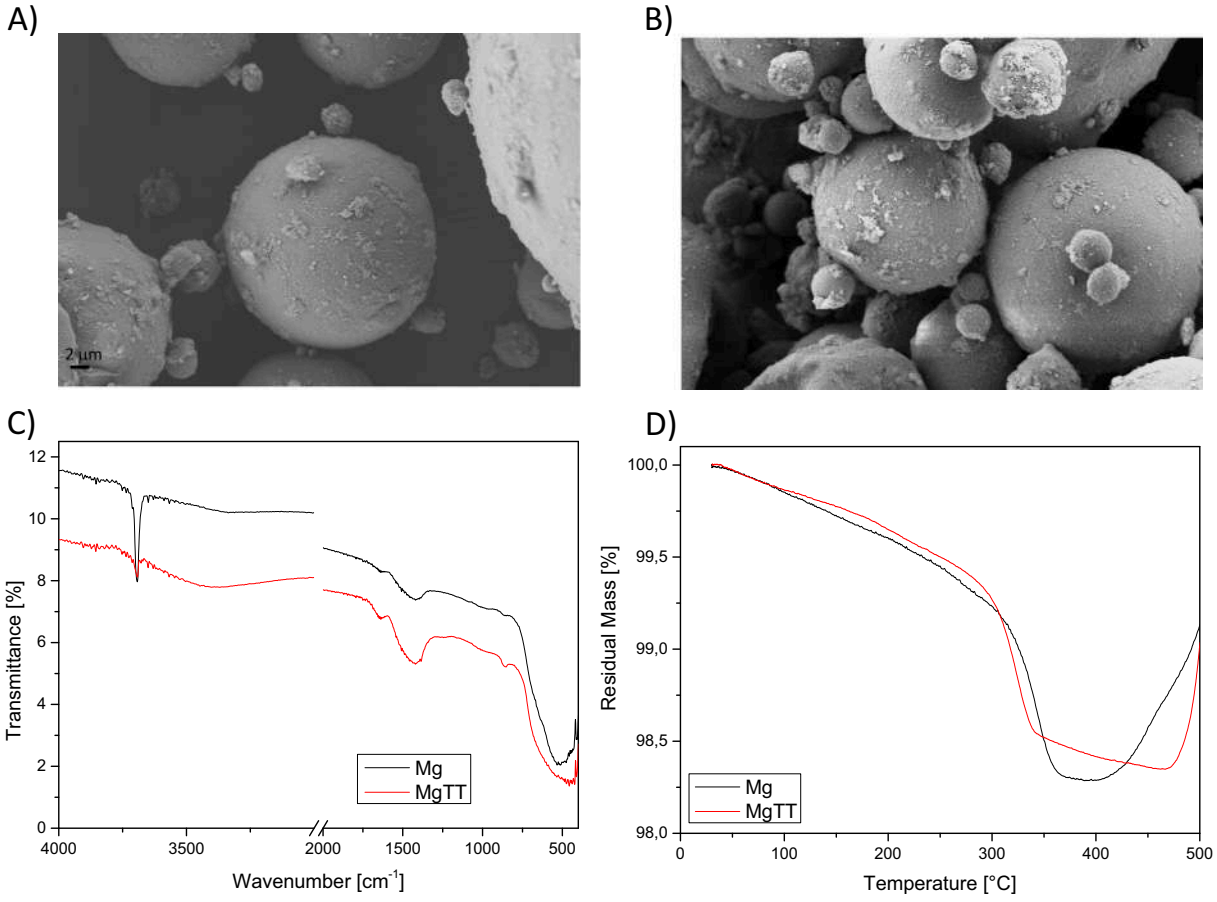

Fig. 1. FESEM images of Mg particles (A) and thermal-treated Mg particles (B). Infrared spectra (C) and residual mass (D) of Mg and MgTT particles.

to modify the surface layer of the Mg particles [38], that can affect the interface properties and the final composite films. TGA shows a different degradation behavior in nitrogen atmosphere (Fig. 1D). The proposed reaction due to the thermal treatment is

$$Mg(OH)_2\ (s) \rightarrow MgO\ (s) + H_2O\ (g)$$

The oxide lamellae typically nucleate and grow from the parent hydroxide lamella until complete dehydration. During dehydration, the oxyhydroxides nucleate and grow and subsequently yield oxides [35].

3.2. Masterbatch characterization

Next, we analyzed the morphological and chemical properties of PLA/MgPEI masterbatch granules (Fig. 2). Fig. 2A shows a picture of PLA/MgPEI granules whose cross section has been analyzed by using scanning electron microscopy. SEM images reveal that Mg particles are dispersed along with the composite granules with a highly homogeneous distribution in the polymeric phase: Mg particles are embedded in the polymer and wholly covered by a PLA layer (Fig. 2B, C). This polymer distribution around the particles is due to the Mg particle modification with PEI that enhanced the nucleation effect of metal particles on the PLA during solvent evaporation. The PEI creates an appropriate interface between PLA and Mg particles improving the dispersion of the metallic phase.

DSC analysis in Fig. 2D shows the high increase in the crystallinity when the Mg particle was incorporated. First, the colloidal processing of PLA and PLA/MgPEI composites granules and lately the solvent evaporation increases the crystalline fraction of both materials, since the as-received PLA was amorphous. This phenomenon, described previously by Ferràndez-Montero and co-authors [39] is heightened by the surface modification of the Mg particles with PEI that increased the compatibility of Mg particles with the PLA matrix and enhanced the nucleating effect of the particles. Consequently, the PLA/MgPEI presents a higher T_m (from 147 to 155 °C with the Mg addition) due to the high content of the crystalline fraction (from 3 % of PLA to 36 % of PLA/30MgPEI) (Fig. 2D).

TGA measurements provide further information on PLA modification after the MgPEI particle addition, and about the actual inorganic fraction of the composites. The TGA and derivative thermogram curves are shown in Fig. 2E. In detail, (i) the initial degradation temperature changes from 298 to 198 °C, (ii) the maximum degradation temperature was reached from 351 to 239 °C whereas the final degradation temperature was measured from 361 to 246 °C with the Mg addition, and (iii) the percentage of residual mass (predominantly Mg) was 33 %. These results showed that Mg induces the degradation of the PLA, decreasing the degradation temperatures to 100 °C. This behavior has been associated with the MgO, present on the surface of the Mg particles, that acts as a catalyst for the PLA depolymerization reaction when the polymer is subjected to elevated temperatures. This effect can be used to tune and modulate the degradation behavior of the PLA by using increasing content of Mg particles.

The FT-IR spectrum of the masterbatch in the 2000–500 wavenumber region (Fig. 2F) shows the typical peak of the PLA, PEI and Mg particles. In particular, the C═O stretching vibration at 1755 cm^{-1} due to PLA polymer with a band at 1722 cm^{-1} that can be attributed to PEI polymer. The band at 1624 cm^{-1} and 1356 cm^{-1} can be due to N—H and C—N stretching vibration mode of PEI, while a large band is present in the 800–400 cm^{-1} region expected for the stretching vibration of Mg—O bond.

3.3. Polymer and composite film characterization

Homogenous, flexible, free-standing PLA-based films were successfully obtained after the extrusion process, with the selected process parameters. The presence and content of Mg particles had an impact on the transparency, colours, roughness, mechanical and thermal

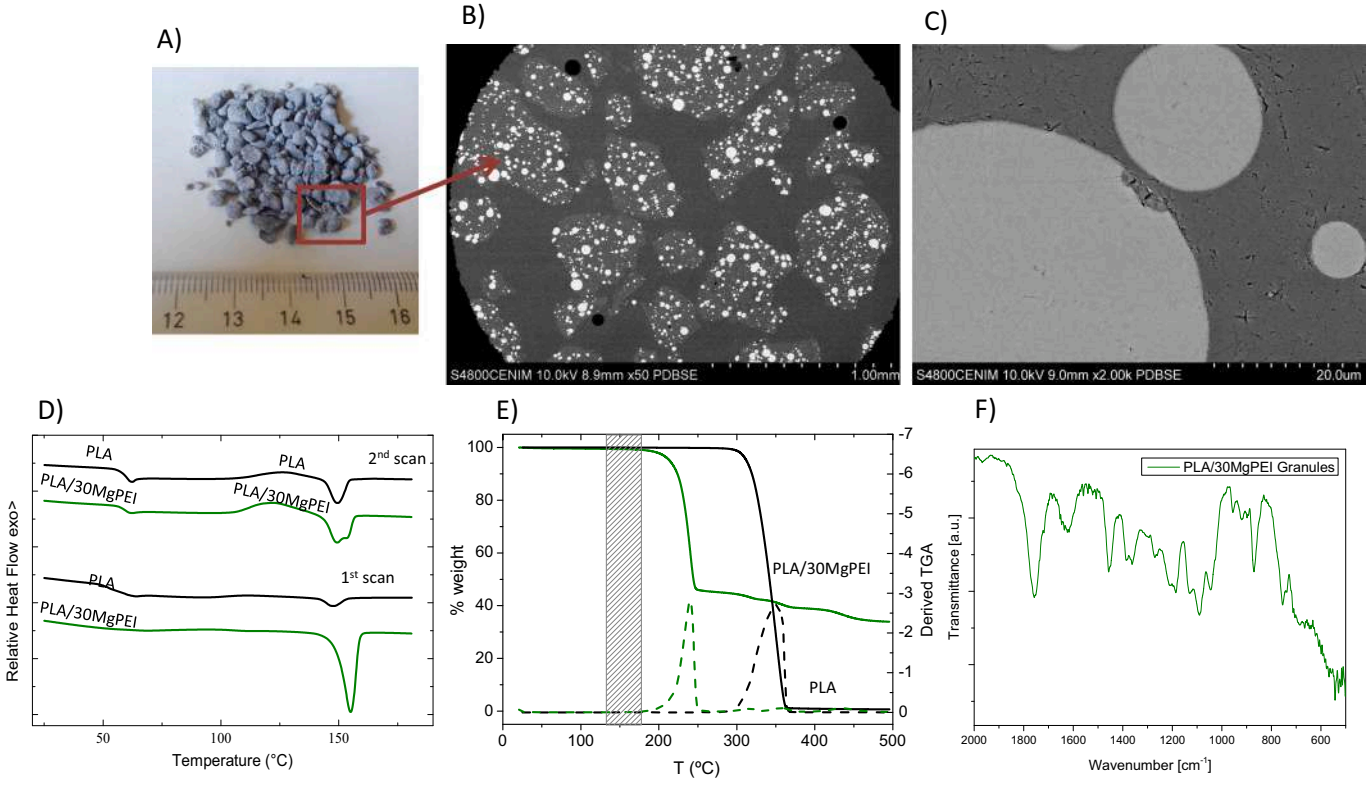

Fig. 2. Image of PLA/30MgPEI composite granules (A) and cross section electron microscope image (B, C), DSC (D), TGA analysis (E) of PLA and PLA/30MgPEI composite and FT-IR spectrum of PLA/30MgPEI granules (F).

properties of the PLA films. Infrared spectra were also performed on PLA and composite films (Fig. S1), displaying the typical band of PLA and PEI. No significant differences are revealed between the PLA and composites at the selected Mg weight content.

3.3.1. Mechanical analysis

Tensile tests were performed to evaluate the effect of the presence, content, and surface treatment of Mg particles on PLA polymer films. PLA-thermal-treated and -PEI-modified Mg particles were analyzed and compared with pristine PLA. Fig. 3 showed histograms of stress at yield (Fig. 3A), Young Modulus (Fig. 3B), strain at maximum strength (Fig. 3C) at 5 and 10 wt% content of different modified Mg particles, and representative stress-strain curves of PLA/Mg composites at 5 wt% content of each Mg type (Fig. 3D). Young modulus of the composites (Fig. 3B, Table 3) had a slight decrease with respect to the PLA films, at low (5 wt%) Mg content, while the decreasing results are more marked in the composite with the highest Mg content (10 wt%). This trend was confirmed also by the tensile strength and strain histograms (Fig. 3A and C) for all Mg particles.

Samples with 10 wt% Mg particles showed a marked decrease both in stress and strain values, measured at yield, which suggested an excess of the microparticles that are not well-performing in mechanical behavior (Fig. 3A and C).

All PLA-based films show the same behavior for the stress-strain curve (Fig. 3D), with a maximum at the yield point followed by a cold-flow region and finally, failure, which is typical for ductile polymers [30]. Mg particles affect the elongation at break which decreases by increasing the Mg particles and strength. At 10 wt% of Mg content, the strength values were lower because the high level of Mg in the composite does not allow the good dispersion of the particles, also due to the presence of particle agglomerates, hindering the formation of an effectual interface between matrix and filler. We next investigated the influence of interfacial matrix/particle adhesion on the mechanical properties of PLA micro-composites. The film with PEI modifications showed the highest Young modulus value of composites, suggesting that this performance can be associated with an improving interfacial adhesion between the polymer matrix and the metal microparticles induced by PEI (Table 3, Fig. 3B). Similar values were obtained for MgTT particles.

Based on the mechanical property results, films with 5 wt% content were selected to compare and evaluate the effect of Mg presence or modification on osteoconductive properties to stem cells.

3.3.2. Morphological characterization

To analyze the integration of the Mg particle in the PLA matrix, FESEM analysis was also performed on the cryo-fracture surface of the films. Electron microscopy images (Fig. 4A–H) revealed Mg particles uniformly distributed in the PLA polymer matrix, and a distinct microroughness induced on the surface by the presence of the individual magnesium particles. Multiple Mg particles were dispersed on the surface and in the interior of the composite. No apparent aggregation and cracks were observed. However, in the cross-section of PLA/5Mg

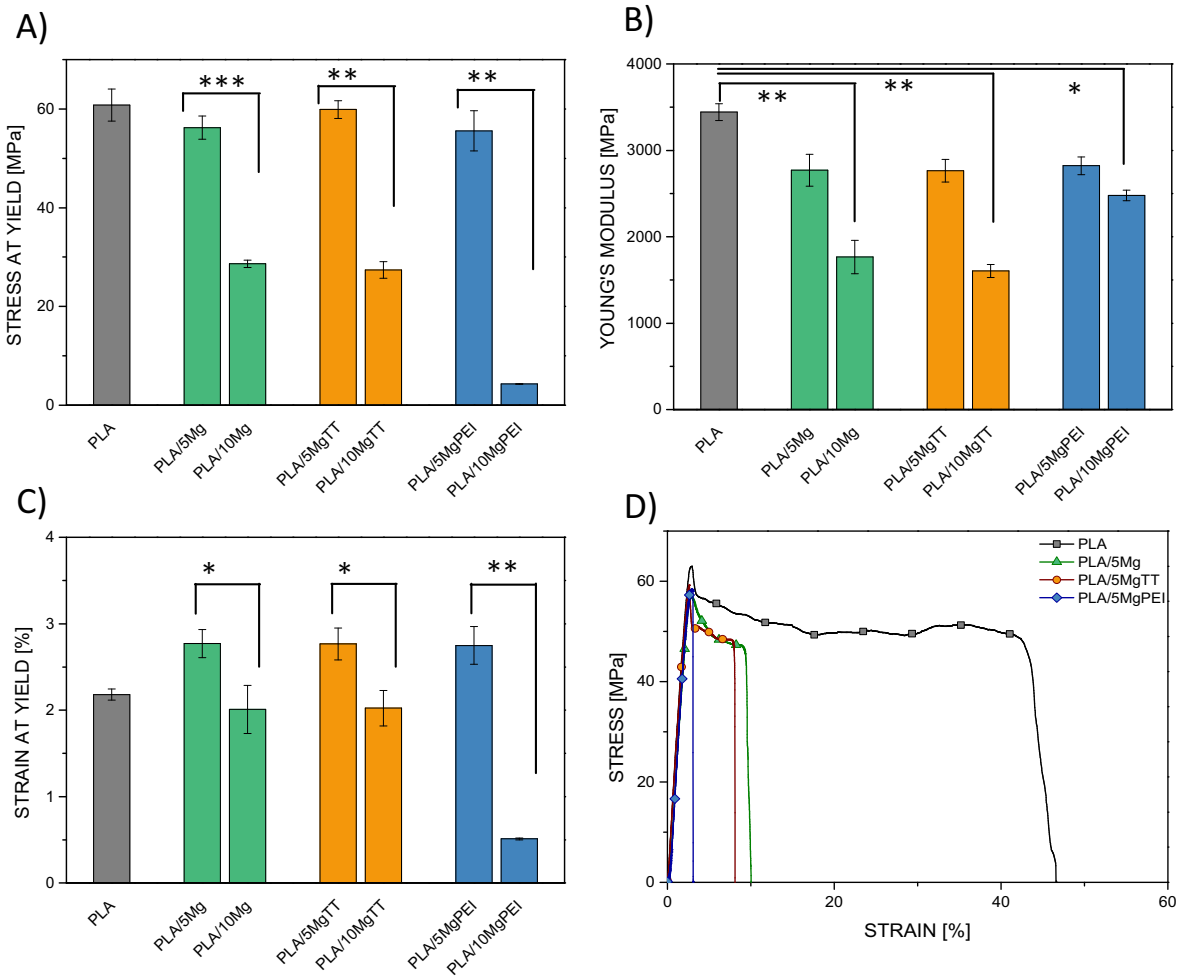

Fig. 3. Mechanical Properties of PLA and PLA-based composites: stress at yield (A), Young Modulus histograms (B), strain at maximum strength (C) and representative stress-strain curves of PLA composites ad 5 wt% weight content and different Mg type at the same Mg content (D).

Table 3
Thermal, mechanical, and surface properties of PLA and composites based on magnesium particles.

Materials	DSC Second heating scan			TGA	Tensile test			Surface properties
	T_g (°C)	T_{cc} (°C)	T_m (°C)	T_d (°C)	σ_Y (MPa)	$\varepsilon_{\sigma Y}$ (%)	E (GPa)	WCA (°)
PLA	56.0 ± 0.1	118.5 ± 0.9	148.3 ± 0.5	317 ± 1	61 ± 3	2.18 ± 0.06	3400 ± 100	78.6 ± 1.1
PLA/5Mg	55.8 ± 0.7	121.9 ± 0.1	148.9 ± 0.1	294 ± 1	56 ± 2	2.77 ± 0.16	2770 ± 180	74.4 ± 0.4
PLA/5MgTT	54.2 ± 1.9	122 ± 4	148 ± 1	308 ± 1	60 ± 2	2.77 ± 0.18	2770 ± 130	75.6 ± 0.7
PLA/5MgPEI	55.5 ± 0.1	128.4 ± 0.3	149.8 ± 0.1	284 ± 2	56 ± 4	2.75 ± 0.21	2820 ± 100	71.8 ± 0.9

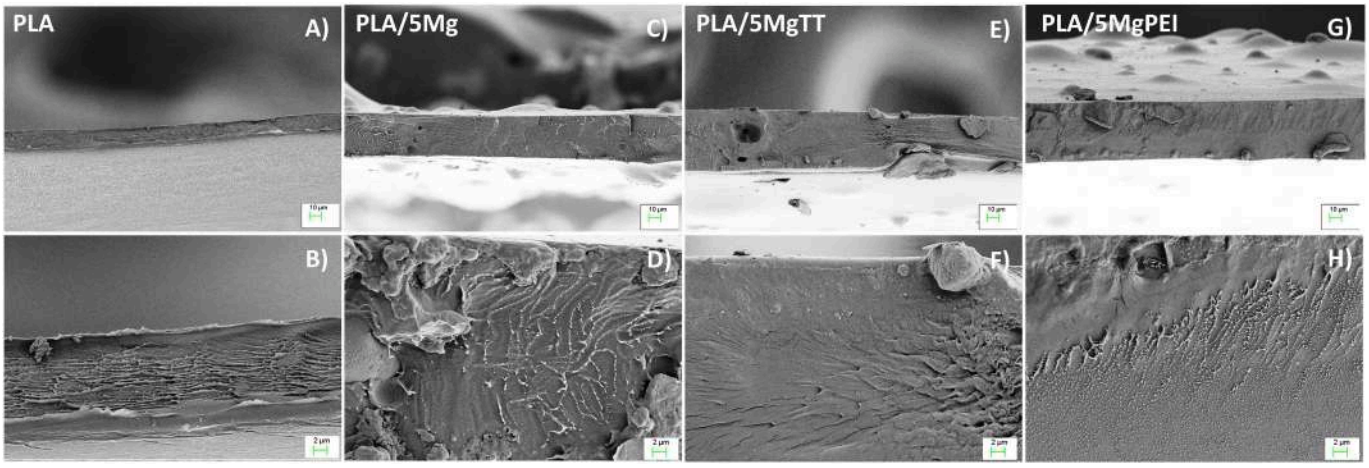

Fig. 4. FESEM images of the fracture surface of PLA (A, B), PLA/5Mg (C, D), PLA/5MgTT (E, F) and PLA/5MgPEI (G, H) composites at different resolutions. Arrow lines in panel D indicate the presence of empty holes in the cross-section of PLA/5Mg composite.

samples we observed the lack of particle-polymer adhesion in some empty holes from the pull out of Mg particles during the fracture (Fig. 4D). In the Mg particles treated composites, this phenomenon is not clearly observed.

3.3.3. Thermal characterization

Fig. 5 shows the residual mass (A) and DTG (B) curves of PLA and composite films. This technique demonstrated that no detectable impurities were present in the composite samples. All films have a pronounced thermal degradation peak, which is attributed to the decomposition of polymers (PLA and PEI) whose temperatures (240–290 °C) decrease with the increase of Mg particle content in the composites (data not shown). The temperature at maximum degradation rate (T_d) followed a similar trend to T-5 %, decreasing from 317 °C for pure PLA to 283 °C for PLA/5MgPEI (Fig. 5A). TGA permitted to underline the different behaviors of the presence of Mg and surface treatment at the same Mg particle content. Mg particles in the PLA reduced the maximum thermal degradation temperature. This is caused by the MgO present on the surface of the Mg particles, that acted as a PLA depolymerization agent at high temperatures [40]. Fig. 5A shows this effect mainly in pristine Mg and PEI-modified particles. The higher thermal stability of PLA/5MgTT composite films can be due to the dehydration of the $Mg(OH)_2$ phase precipitated on the Mg particles and, therefore, the formation of crystalline MgO, as previously observed [36].

Since PLA is a semicrystalline polymer, its mechanical properties depend largely on its original crystallization state. Fig. 5 presents 1st (C) and 2nd (D) heating DSC curves of PLA and PLA-based composites at 5 wt% filler content for the different kinds of magnesium particles. Thermal properties are summarized in Table 3.

All films exhibited the crystallinity degree (X_c), calculated based on the enthalpy of fusion of 100 % crystalline PLA, which is 93 kJ/g [30], <2 %. All films have a glass transition temperature, a cold crystallization temperature, and a melting temperature. The neat PLA film is characterized by a T_g at 56 °C, a T_{cc} at 118.5 °C, and finally a T_m at 148.3 °C. The addition of 5 wt% Mg particles to the neat PLA resulted in an increase in T_{cc} up to 10 °C. This effect is more evident in the case of PEI-modified Mg particles. Cold crystallization peaks are retarded and sharper in the composites; the delay (formation at higher temperatures) may be due to the thermal inertia of the metal particles which function as heat absorbers and accumulators; the sharped form could depend both on the release of the accumulated heat and on the nucleating effect of the particles for the formation of crystals. The formation of crystals of more uniform temperature by nucleation is also confirmed in the initial shape of the melting peak which appeared more gradual in PLA and more sloping in composites. This can be attributed to the restriction of the mobility of the polymer chains as the consequence of the interface properties on the Mg particle surface.

3.3.4. Wettability

Wettability property influences the interaction of the material and cells or biological fluids [22,30,41]. Fig. 6 displayed the Water Contact Angle (WCA) measurements of PLA and Mg particles-based composites, and the comparison between different content and types of Mg particles. The Mg particle surfaces modify slightly the WCA values of the composites, thus improving the hydrophilic properties of the PLA film (Fig. 6A). This effect was induced by the changes in both physical and chemical surface properties of the PLA film for the dispersion of the Mg particle [8]. According to previous studies from some of our co-authors [8,42], hydrophilicity is connected with the chemical constitution of the composite, microstructure and roughness. A decrease in the WCA values by increasing the Mg content was observed ranging from 79° for PLA film to 69° for PLA/10Mg particles (Fig. 6B). These studies indicated that the WCA changes in composite films can be attributed to (i) the hydroxyl groups exposed on the surface of Mg particles, which can form hydrogen bonds with water; (ii) the higher specific surface area of the composite respect to PLA.

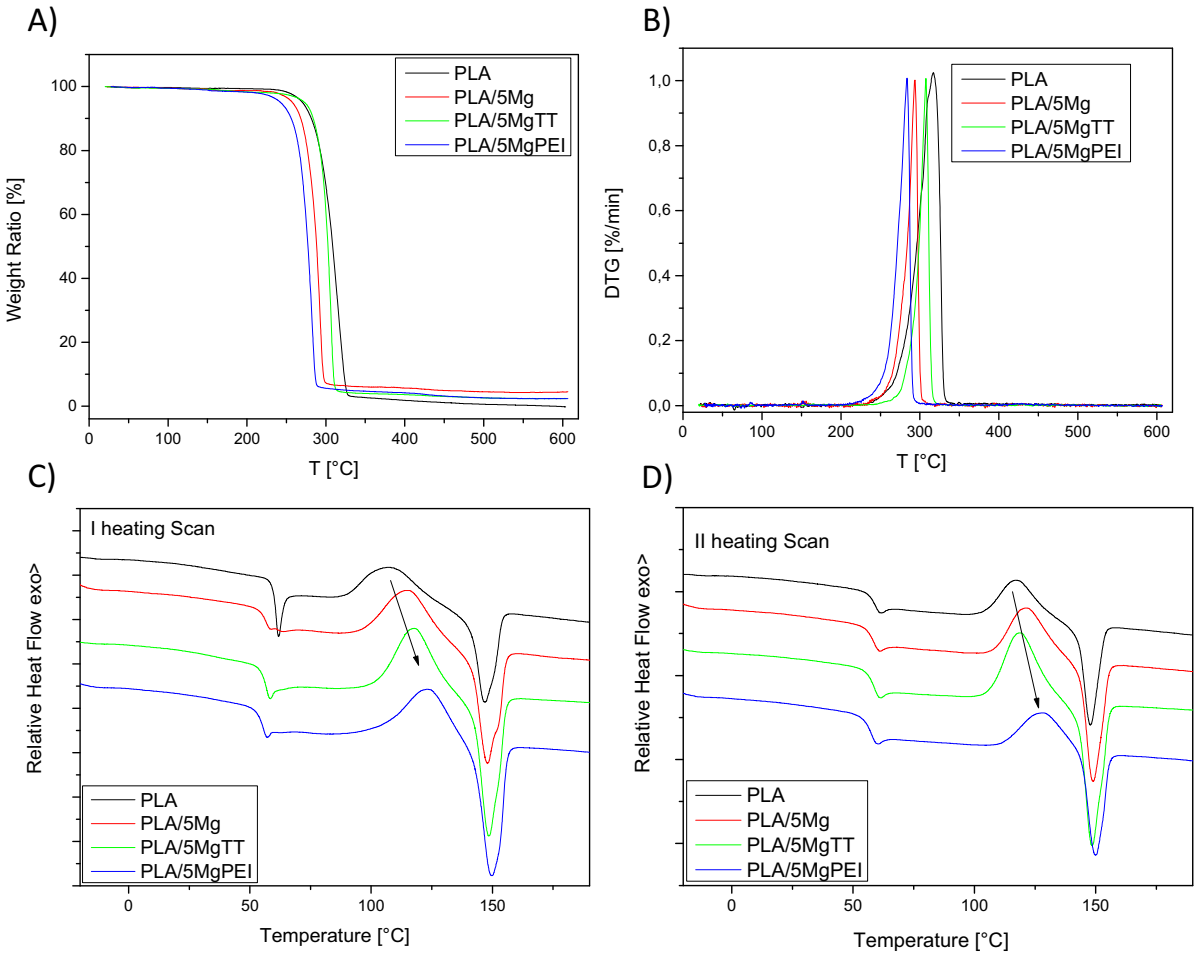

Fig. 5. (A) TG and (B) DTG curves of PLA and composite films. DSC thermograms of PLA, and composites at the first (C) and second (D) heating scan.

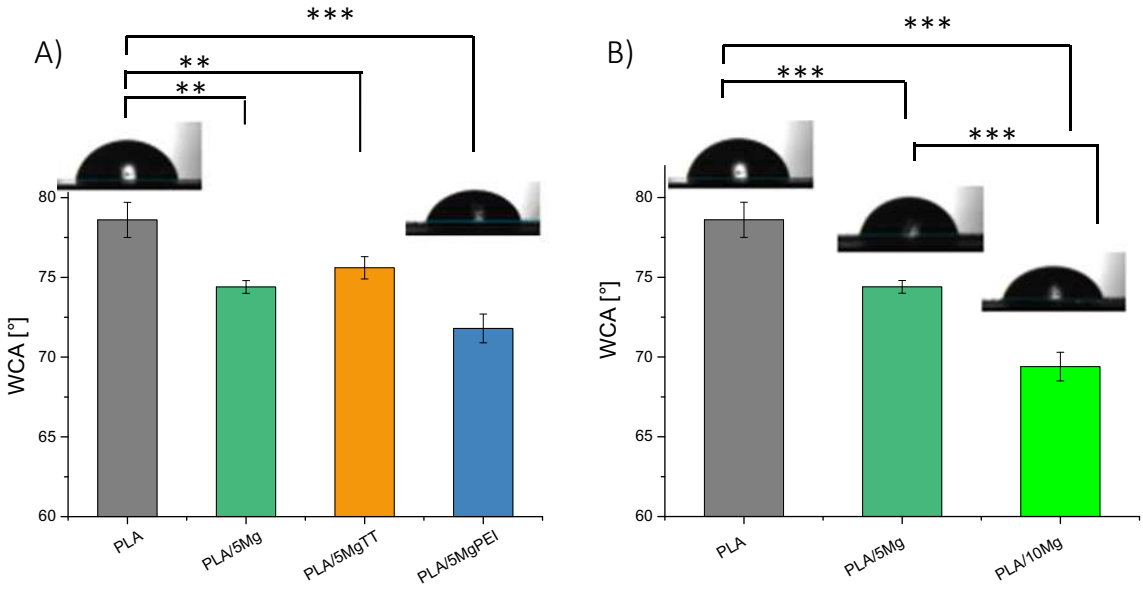

Fig. 6. Water contact angle measurement of Mg-based composites. (A) Role of the different treatments in composite films; (B) role of the Mg content in PLA polymer matrix.

3.3.5. Protein adsorption

Finally, we measured the capability of neat and Mg-composites PLA films to interact with the proteins. We performed the protein adsorption assay according to our previous works [22,23].

Histograms in Fig. 7 showed a similar protein adsorption capability of PLA/5Mg- and PLA/10Mg-based films, and a general increase of the absorbed proteins when compared to neat PLA. We measured a comparable amount of the selected proteins' samples after 30 min and 24 h of incubation, suggesting that the film surfaces are rapidly saturated by the bonded proteins, although with some difference among PLA/Mg-derivative films (Fig. 7A, B). Compared to neat PLA, the adsorption of the plasma proteins was highest on PLA/5MgTT, PLA/10MgTT, PLA/5MgPEI, and PLA/10MgPEI (Fig. 7A, B), while the adsorption of FBS 2 % and FBS 10 % was highest on PLA/5MgPEI and PLA/10MgPEI (Fig. 7A, B).

No differences we detected in the amount of adsorbed BSA between all PLA/Mg composites although we observed a general light-increased trend compared to neat PLA film (Fig. 7A, B). These results indicated that the presence of Mg particles in combination with the two treatments improves the binding of proteins with respect to neat PLA polymer. The highest values on PLA/5MgPEI may be due to the lowest WCA measurements that correlated with an increase in wettability (Fig. 6).

3.4. PLA/Mg composite films are suitable for the culture of hASCs

First, we investigated whether PLA, PLA/5Mg, PLA/5MgTT, and PLA/5MgPEI polymer films were suitable for hASCs culture (Fig. 8). We selected the PLA polymer films containing 5 wt% Mg for the hASCs culture based on the mechanical property (Fig. 3) and the comparable adsorption capability of the films' surface between 5 wt% Mg and 10 wt % Mg (Fig. 7).

hASCs have a mesenchymal origin and are recognized to be one of the most suitable stem cell types for tissue engineering-based applications due to the relatively standardized and easy method of isolation, the well-established procedures for *in vitro* expansion and differentiation toward cells of non-hematopoietic lineages, such as fibroblasts, osteocytes, adipocytes, chondrocytes, and neural cells [3], and for their immunomodulatory activity that allows recreating the stem cell microenvironment [4,43].

In these sets of experiments, hASCs were seeded on neat PLA, PLA/5Mg, PLA/5MgTT, and PLA/5MgPEI polymer films in the growth culture medium (Fig. 8A). As experimental controls (CTR), hASCs were seeded on TCP/glass coverslip in the growth culture medium (Fig. 8A). Stem cell viability (MTT assay) (Fig. 8B) and cell morphology (immunofluorescence, IF) (Fig. 8C) were evaluated at different time points (3, 7, 14, 21, and 30 days) of the culture (experimental plan in Fig. 8A). We observed a similar mitochondrial dehydrogenase activity curve of hASCs on PLA and PLA/Mg-based films, demonstrating the biocompatibility of the materials (Fig. 8B). Next, we analyzed the effect of PLA and PLA/5Mg-based films on stem cell morphology (Fig. 8C). Immunofluorescences displayed a comparable organization of the cytoskeleton components, F-Actin microfilaments and Microtubules, in hASCs seeded on PLA and PLA/5Mg composite films (Fig. 8, representative images at selected time points), depicting a canonical fibroblast-like morphology matching that of hASCs cultured in canonical control culture condition. More in detail, the tubulin-positive fibers (Microtubules, red) radiate out from the organizing center beside the nucleus, while the F-Actin–containing fibers (green) are arranged as straight, cable-like cords that cross the cytoplasm in different directions but are preferentially oriented along the main cellular longitudinal axis (Fig. 8C).

Together these data demonstrated that these polymers are suitable for stem cell culture, even for a long-term culture (Fig. 8B, C).

These results were confirmed by FESEM analyses that highlighted the interaction of hASCs with the surface of PLA and PLA/5Mg-based films. High magnification FESEM images revealed some differences between systems, with stem cells that emitted thin filopodia on PLA/5MgPEI and large lamellipodia on PLA/5MgTT and PLA/5Mg, perhaps as an effect of the surface microstructure of PLA/Mg composite films that showed a microroughness induced by Mg dispersion in the film (Fig. 9).

3.5. Osteogenic differentiation induction of PLA/Mg-based films on hASCs

Due to the osteoinductive properties of Mg particles [8–10,14,44], next, we investigated the osteogenic differentiation of stem cells cultured on each PLA and composite polymer film in the growth culture medium without osteogenic inducers (Fig. 10A). The cells were collected after 21 days of culture, the estimated time point necessary for obtaining the osteogenic differentiation of hASCs *in vitro* after treatment with the

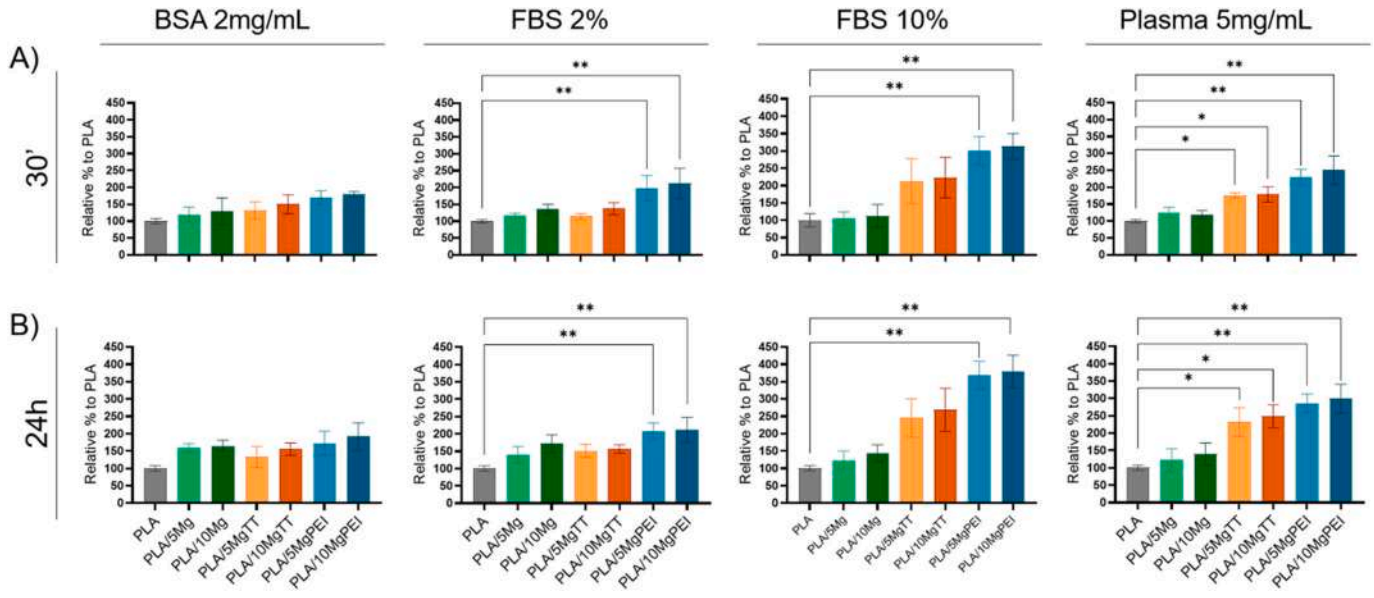

Fig. 7. Adsorbed protein on PLA, and PLA/5Mg, PLA/10Mg, PLA/5MgTT, PLA/10MgTT, PLA/5MgPEI and PLA/10MgPEI. (A) Total adsorbed proteins (absorbance 595 nm) from BSA, FBS and plasma after 30 min at 37 °C and (B) after 24 h at 37 °C. The data are reported in percentage with respect to the PLA as mean ± SD. Significance of the differences was indicated as follows: $*p < 0.05$; $**p < 0.01$.

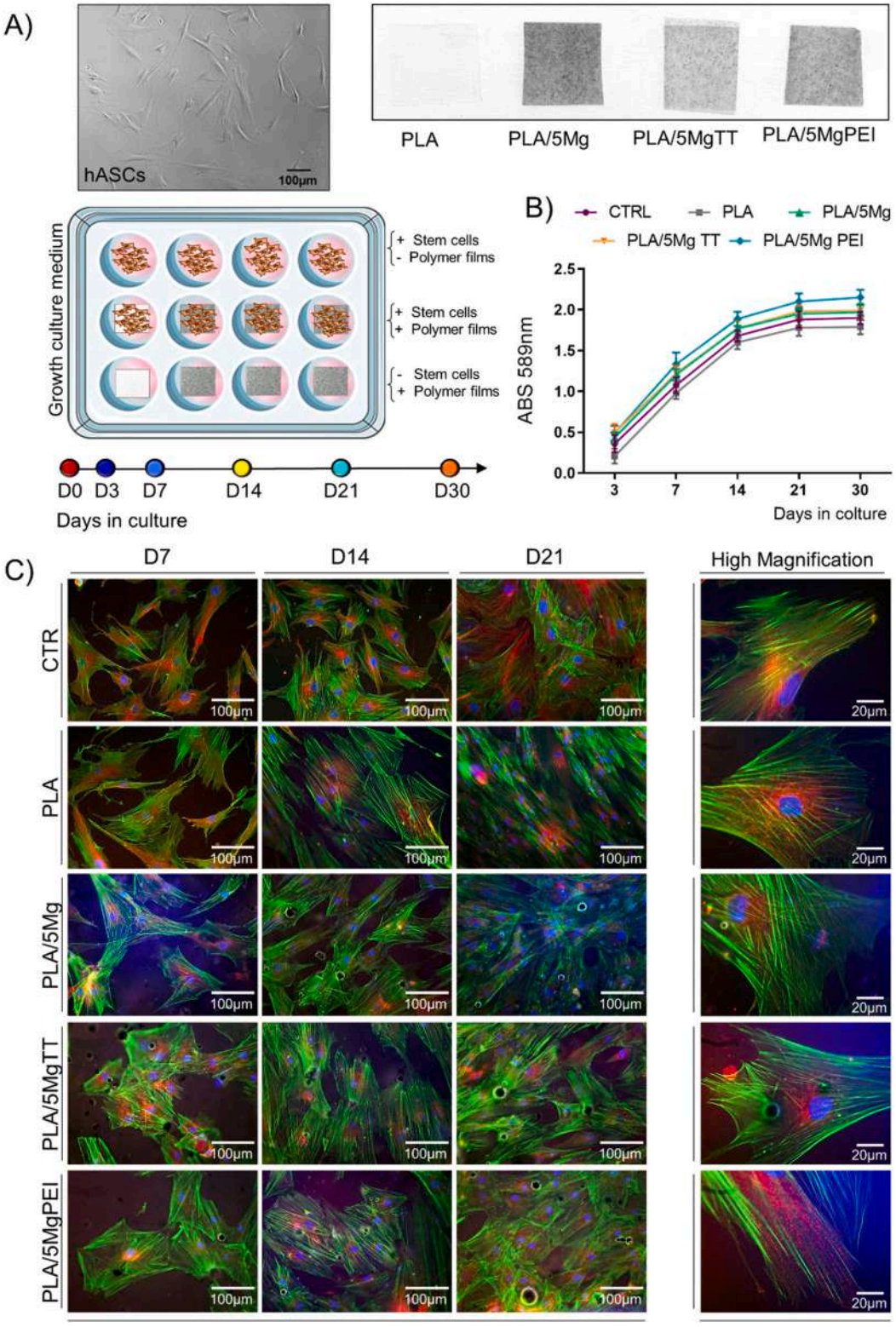

Fig. 8. Viability and morphology of hASCs on CTR, PLA, PLA/5Mg, PLA/5MgTT, PLA/5MgPEI. (A) Schematic representation of experimental plan: on the left representative brightfield image of h-ASCs on TCP, scale bar = 100 μm; on the right representative photos taken with a Canon Powershot S200 camera demonstrated the optical transparency of neat PLA compared to optically non-transparent PLA/Mg-based films due to the presence of Mg. hASCs were seeded on neat PLA and on PLA/Mg-based films in the growth culture medium for 30 days. In parallel, controls included the culture of stem cells on TCP/glass coverslip in the growth culture (CTR). The films without stem cells were also evaluated. (B) MTT assay of hASCs on PLA, PLA/5Mg, PLA/5MgTT and PLA/5MgPEI films and on canonical culture conditions (TCP) at 3, 7, 14, 21 and 30 days. Data are representative of three independent experiments which yielded similar results. (C) Representative fluorescence images of nuclei (4′,6-diamidino-2-phenylindole, DAPI, blue), F-Actin (Alexa-fluor-488 Phalloidin, green), and β-Tubulin (anti-Tubulin antibody, red) at 7, 14 and 21 days, were acquired with fluorescence microscopy Eclipse-TE2000-S, Nikon using the F-View II FireWire™ camera (Soft Imaging System, Olympus). Scale bar = 100 μm; High magnification scale bar = 20 μm.

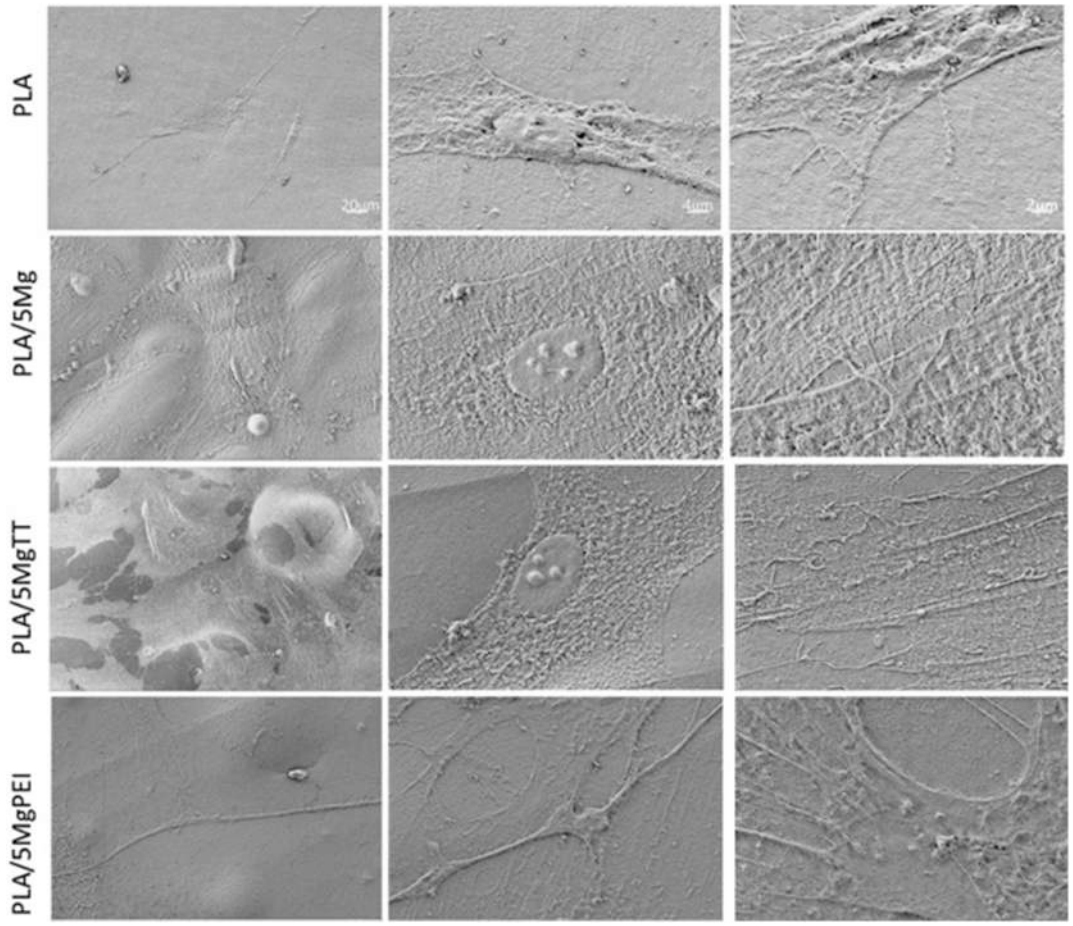

Fig. 9. FESEM Images of hASCs on PLA and PLA-based Mg composites at different magnification at 7 days of culture.

osteogenic differentiation medium [24,28] in TPC/GC (CTR+) (Fig. 10A). We also seeded hASCs on TCP/glass coverslips in the growth culture media for the same time as the negative experimental control (CTR−). The interference of polymer films without stem cells was also evaluated (Fig. 10A).

After 21 days in the above culture conditions, cells were analyzed for the expression of osteogenic markers: Calcium deposit, Alkaline Phosphatase activity (ALP), type I Collagen (COL.1), and Osteopontin [also known as Secreted Phosphoprotein 1 (SPP1)] (Fig. 10B–D); and RUNX2, SPP1, and Bone Gamma-Carboxyglutamate Protein (BGLAP) genes (Fig. 10E). Lipidomic analysis was also performed (Fig. 11).

3.5.1. Osteogenic differentiation markers are expressed in hASCs-PLA/Mg cultures

Osteoblasts overexpress ALP, an enzyme that covers a key role in bone mineralization processes by the cleavage of pyrophosphate (mineralization inhibitor), allowing calcium hydroxyapatite deposition in matrix bone formation [45].

As expected, due to the osteogenic differentiation of hASCs, the staining of ALP was highly positive in stem cells cultured with the osteogenic differentiation medium (CTR+, Fig. 10B). In contrast, it was undetectable in stem cells grown in canonical culture conditions (CTR−, Fig. 10B) and in neat PLA and composite polymer films without stem cells (Fig. 10B c′, d′, e′, f′). Of note, we found an increased expression of ALP in hASCs seeded on PLA/5Mg-based films (Fig. 10B d, e, f) with the highest signal in PLA/5MgTT (Fig. 10B e).

These results were confirmed by measuring calcium deposits obtained by incubating the cells with Alizarin Red, the commonly used histologic dye to identify calcium deposits in differentiated osteocytes. We obtained positive staining in hASCs seeded on polymer films in this order: PLA/5MgTT > PLA/5Mg > PLA/5MgPEI > PLA (Fig. 10B i, j, k, l; Fig. 10D) and in stem cells cultured with osteogenic medium (CTR+, Fig. 10B h; Fig. 10D), whereas the staining was absent in films without stem cells (Fig. 10B i′, j′, k′, l′; D) and in stem cells in growth culture medium on TCP (CTR−, Fig. 10B g; D).

Further evidence of the higher PLA/5MgTT osteoinductive potential with respect to the other PLA/5Mg-based films were from the evaluation of two specific osteogenic markers, Osteopontin and type I Collagen (Fig. 10B o, p, q, r; Fig. 10B u, v, w, x). Osteopontin is a glycophosphoprotein synthesized by osteoblasts [46]. It is a non-collagenous protein of the bone matrix and binds strictly to calcium hydroxyapatite, assuming an essential role in responses to external stresses and bone maintenance. Type I Collagen, secreted by osteoblasts, is one of the major structural components of the organic bone matrix. Bone tissue is responsible for almost the entire synthesis of type I Collagen, therefore type I Collagen is a strong marker of bone formation [47,48].

The expression of Osteopontin and type I Collagen confirmed the major osteogenic inducing potential of PLA/Mg-based films toward the differentiation of hASCs (Fig. 10B, C). Moreover, the high magnification images in Fig. 10C revealed a comparable architecture in the extracellular environment of the type I Collagen signal in cells on PLA/5MgTT's and CTR+.

Finally, hASCs cultured on PLA/5Mg-based polymer films in a growth culture medium expressed the highest levels of RUNX2, BGLAP, and SPP1 genes with respect to stem cells cultured on TCP (Fig. 10E). The level of these osteogenic genes was, however, higher in stem cells cultured in an osteogenic differentiation medium (Fig. 10E). Interestingly, in neat PLA-stem cell cultures, we observed an increased expression of the SPP1 gene (Fig. 10E), indicating the role of the polymer firm composition in dictating changes in the stem cell fate but also

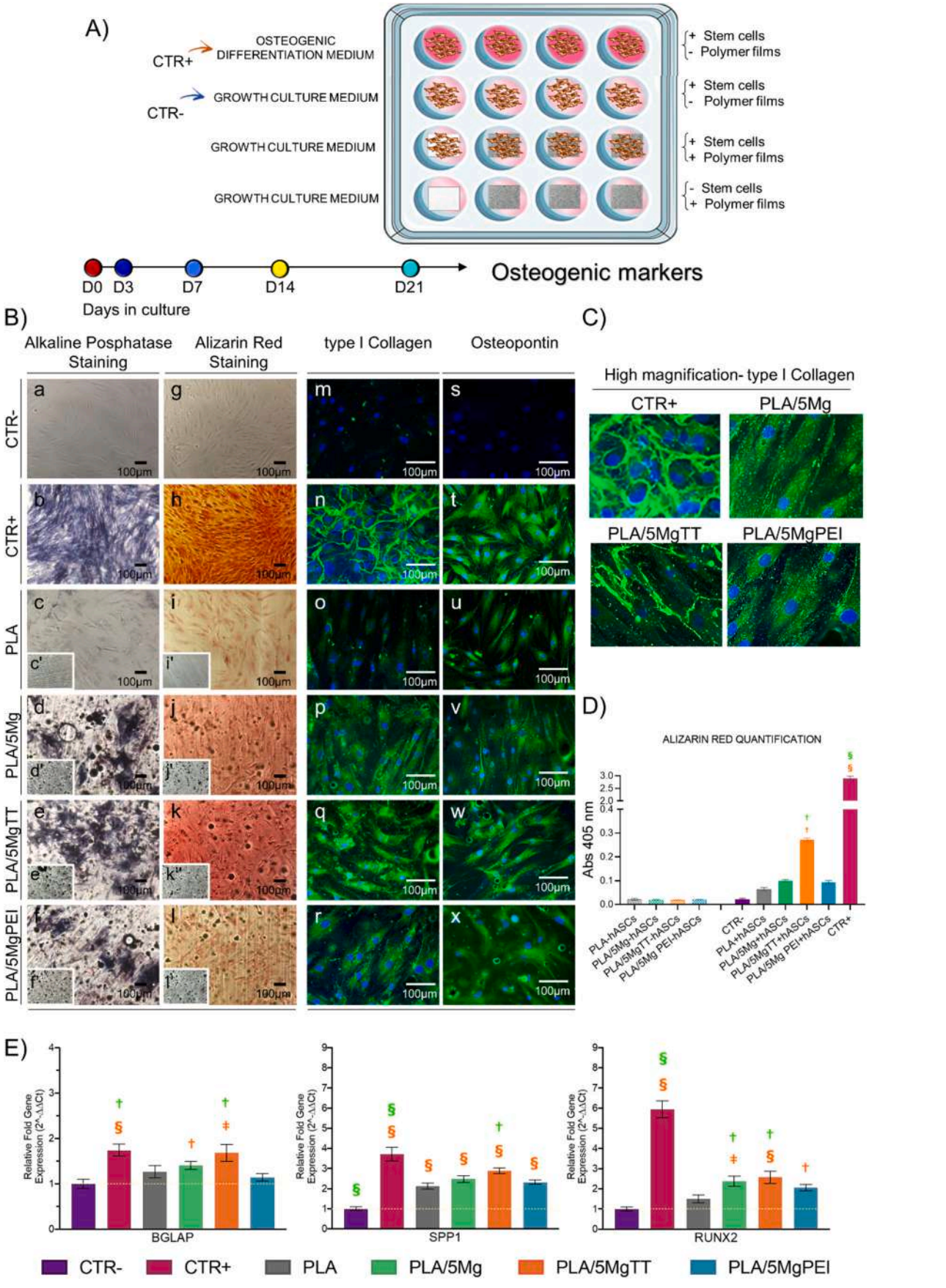

(caption on next page)

Fig. 10. Osteogenic differentiation of hASCs on PLA, PLA/5Mg, PLA/5MgTT, and PLA/5MgPEI. (A) The experimental plan is shown schematically: CTR+, stem cells were grown with osteogenic differentiation medium; CTR−, stem cells were cultured on TCP/glass coverslip in growth culture medium; hASCs were seeded on neat PLA and PLA/5Mg-based films in growth culture medium. The interference of films with medium without stem cells was also evaluated. All systems studied were maintained for 21 days in culture. (B) Representative brightfield images of Alkaline Phosphatase Staining of hASCs seeded on TCP using growth culture medium (CTR−) (a) of hASCs differentiate toward osteocyte *in vitro* condition using a differentiation osteogenic medium (CTR+) (b) of hASCs cultured on PLA and PLA/5Mg-based films using growth culture medium (c, d, e, f), and of materials without the stem cells (c′, d′, e′, f′). Representative brightfield images of Alizarin red staining of hASCs on TCP (CTR−) (g) of hASCs differentiate toward osteocyte *in vitro* condition (CTR+) (h) of hASCs cultured on PLA and PLA/5Mg-based films (i, j, k, l), and on respectively film without the stem cells (i′, j′, k′, l′). Scale bar = 100 μm. Representative fluorescence images of type I Collagen (anti-type I Collagen, green) and nuclei (4′,6-diamidino-2-phenylindole, DAPI, blue) of hASCs maintained in canonical culture conditions (m) of hASCs differentiate toward osteocyte *in vitro* condition (n) of hASCs cultured on PLA and PLA/5Mg-based films (o, p, q, r). Representative fluorescence images of Osteopontin (anti-Osteopontin, green) and nuclei (4′, 6-diamidino-2-phenylindole, DAPI, blue) of hASCs maintained in canonical culture conditions (s) of hASCs differentiate toward osteocyte *in vitro* condition (t) of hASCs cultured on PLA and PLA/5Mg-based films (u, v, w, x). Scale bar = 100 μm. (C) High magnification of fluorescence images of type I Collagen expression in hASCs cultured on PLA/5Mg, PLA/5Mg TT, and PLA/5Mg PEI. Type I Collagen (anti-type I Collagen, green) and nuclei (4′, 6-diamidino-2-phenylindole, DAPI, blue). (D) Quantitative analysis of Alizarin Red Staining (see Materials & methods section for details). The results are reported as mean ± SD of three independent experiments. † = $p < 0.01$; ‡ = $p < 0.001$; § = $p < 0.0001$. Red symbols represent multiple comparison test *vs.* CTR−; Green symbols represent multiple comparison test *vs* PLA. (E) qPCR gene expression of BGLAP, SSP1, and RUNX2 in hASCs cultured on PLA and PLA/5Mg-based films. Results are expressed as mean ± SD of three independent experiments. † = $p < 0.01$; ‡ = $p < 0.001$; § = $p < 0.0001$. Red symbols represent multiple comparison test *vs.* CTR−; Green symbols represent multiple comparison test *vs* PLA.

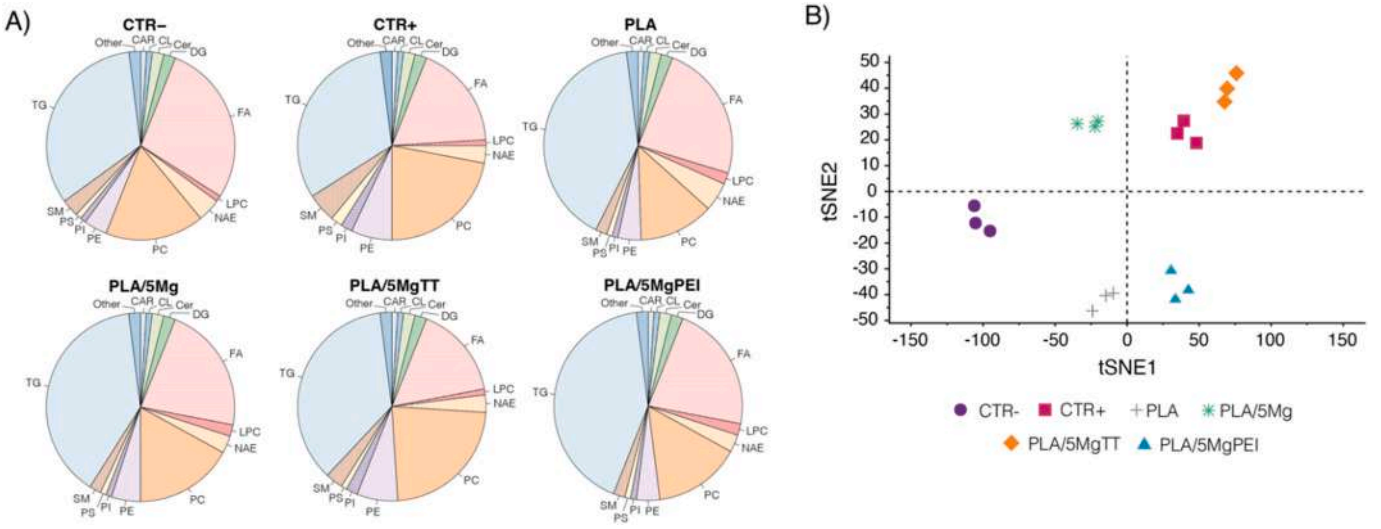

Fig. 11. Lipidomic analysis of undifferentiated hASCs (CTR−), differentiated hASCs (CTR+), and hASCs on PLA, PLA/5Mg, PLA/5MgTT and PLA/5MgPEI. (A) Pie chart showing the percentage of lipid classes analyzed in each system. Acylcarnitine (CAR), Cardiolipin (CL), ceramide (Cer), diacylglycerol (DG), free fatty acid (FA), lyso-PC (LPC), (NAE), phosphatidylcholine (PC), phosphatidylethanolamine (PE), phosphatidylinositol (PI), phosphatidylserine (PS), sphingomyelin (SM), triacylglycerol (TG), Other (see Materials & methods section). (B) t-SNE plot unsupervised comparison of the lipidome in different groups.

highlighting that the PLA-polymer alone is not enough to induce a complete stem differentiation process. Of note, when data are compared to PLA-cultures, only hASCs cultured on PLA/5MgTT expressed the highest levels of RUNX2, BGLAP, and SPP1 genes as stem cells cultured in the osteogenic medium (Fig. 10E).

3.5.2. Lipidomic analysis

The lipidome profile of the plasma membrane during the differentiation of hMSCs toward osteoblasts was evaluated in a recent publication showing a lipidomic remodeling that recapitulated the composition and structure of the plasma membrane of the osteoblasts [49].

We performed a lipidomic analysis in hASCs after 21 days on PLA and PLA/Mg-based in the growth culture medium and related controls (CTR+, CTR−) using a liquid chromatography/mass (LC/MS) QTOF mass spectrometry. Results are reported in Fig. 11. We found a comparable lipid composition between hASCs in osteogenic differentiation medium (CTR+) and hASCs on PLA/5MgTT (Fig. 11A, pie chart). We observed a reduction in the Fatty Acid (FA) lipid class and an increase in phospholipids associated with the osteogenic differentiation, such as phosphatidylcholine (PC), phosphatidylethanolamine (PE), and phosphatidylinositol (PI), mainly in cells on PLA/5MgTT, further enhancing the osteoinductive effect of PLA/5MgTT on hASCs (Fig. 11A). A comparable lipid composition was observed between hASCs cultured in the growth culture medium (CTR−) and hASCs on PLA and on PLA/5MgPEI (Fig. 11A). hASCs on PLA/5Mg showed an intermediate case with a slight reduction in FA and an increase in PC and PE. The lipidome-wide differences between PLA/5Mg-based films were further confirmed by the t-SNE plot of the first two principal components (Fig. 11B). The first two dimensions in the t-SNE plot reveal a distinct difference in the lipidomic profiles between the hASCs cultured in the growth culture medium (CTR−), hASCs cultured in the osteogenic differentiation medium (CTR+), and hASCs cultured on PLA/5MgTT, whereas, the other groups showed an intermediate lipids composition (Fig. 11B).

In conclusion, these results demonstrated that the culture of hASCs on PLA/5Mg films caused the remodeling of the lipid classes with potential osteogenic differentiation involvement. Our findings agree with the previous observation showing the reduction of FA and an increase of PC, PE, and PI during the osteogenic differentiation [49]. Of note, these results highlighted the highest osteoinductive role of MgTT in PLA films, and in general support the role of Mg ions as a cofactor of the enzymes involved in the biosynthesis of the abovementioned lipids [50,51].

To our knowledge, these results are the first to explore the lipidome profile of hMSCs on a biomaterial in the growth culture medium.

3.6. Osteogenic differentiation of hASCs after interaction with PLA-based films

The different effects of the osteoconductive properties of PLA/5Mg composites on stem cells might be directly addressed to the Mg release by the polymer films. For example, in the case of MgPEI, we have demonstrated previously that PEI adsorption stabilizes the Mg phase and decreases the release of Mg to the medium [20]. In contrast, the thermal treatment in the Mg particles induces a faster Mg release from the PLA matrix during the test [52].

Here, we investigated whether osteogenic differentiation required direct contact between stem cells and PLA/5Mg-based films or if the process was dependent on the Mg released in the culture medium. We have co-cultured hASCs with each polymer film for 21 days in the growth culture medium in trans-well plates that separate stem cells and polymer film in the same culture system (Fig. 12A). Positive control (stem cells cultured with osteogenic differentiation medium) and negative (stem cells cultured with growth culture medium) on TCP were included in this set of experiments (Fig. 12A).

On day 21, the cells were stained with alkaline phosphatase to verify the osteogenic differentiation (Fig. 12B).

Images revealed the positive ALP staining in hASCs after 21 days of co-culture with PLA/5Mg-based films (order PLA/5MgTT → PLA/5MgPEI → PLA/5Mg → PLA). On the other hand, no signal was acquired in hASCs in co-culture with neat PLA. As expected, the signal of ALP staining was absent in CTR− (Fig. 12B). These findings demonstrated that the polymer film in culture releases Mg and confirmed that the Mg is osteoinductive (Fig. 12B).

4. Discussion

In this work, we demonstrated the highest osteogenic potential of thermal-treated Mg particles dispersed in PLA toward hASCs.

The PLA/MgTT composite was designed taking into account the osteogenic role of Mg either as a free ion [10,44] or as molecules dispersed in polymer films [7,20,39], as well as the properties of pristine PLA polymer film, that make this polymer of friendly use for tissue engineering approaches [10,15,17,44].

The PLA/MgTT was generated as part of a set of polymeric composite films, consisting of PLA/Mg and PLA/MgPEI, where the Mg was dispersed in the PLA film respectively as Mg particles or Mg particles modified by the adsorption of PEI dispersant in aqueous suspension.

All composites (PLA/Mg, PLA/MgTT and PLA/MgPEI) have Mg particles at two selected contents: wt 5 % Mg or wt 10 % Mg, and were obtained by the extrusion process to guarantee the individual dispersion of Mg particles into the PLA polymer films. In all composites, the inclusion of Mg particles modified the bulk and surface properties of the PLA films. In particular, the Mg wt 5 % decreased the thermal stability of the PLA polymer and restricted the mobility of the polymer chains as a consequence of the interface properties on the Mg particle surface. Moreover, the inclusion of Mg particles preserved the PLA Young modulus, increased the wettability properties of the PLA films and favor

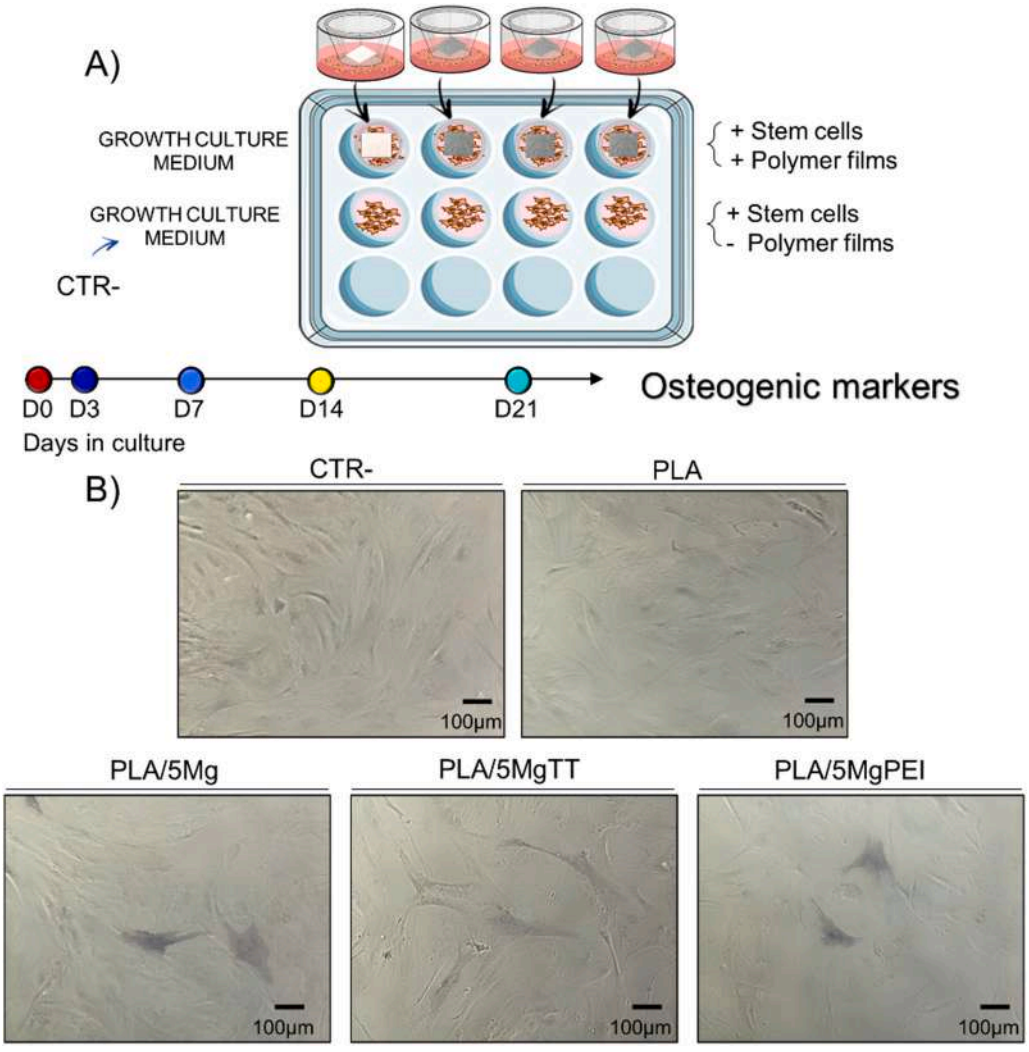

Fig. 12. Osteogenic differentiation of hASCs without the interaction with PLA-based films. (A) The experimental plan is shown schematically: CTR+ stem cells were grown with osteogenic differentiation media; CTR− stem cells were cultured in growth culture conditions; hASCs were co-cultured with neat PLA and PLA/5Mg-based films in the growth culture medium. All systems studied were maintained for 21 days in culture. (B) Representative brightfield images of Alkaline Phosphatase Staining of hASCs in CTR− and CTR+ conditions and of hASCs co-cultured with PLA and PLA/Mg-based films for 21 days. Scale bar = 100 μm. On the right of each photo, the related high magnification of brightfield images was presented.

protein adsorption. Conversely, samples with 10 wt% Mg particles showed a marked decrease both in stress and strain values, and mainly the high level of Mg in the composite does not allow the good dispersion of the particles. Due to the abovementioned characteristics, wt 5 %-based composites were selected for the biological application with hASCs.

All Mg composites (PLA/5Mg, PLA/5MgTT and PLA/5MgPEI) were suitable for the culture of hASCs, as demonstrated by the comparable viability and morphology with the stem cells cultured in the canonical growth culture condition on TCP.

All composites were evaluated for the osteogenic differentiation potential to hASCs in the growth culture condition, in the absence of soluble exogenous inductive molecules, for 21 days (the time needed for the osteogenic differentiation of hASCs with the osteogenic culture medium *in vitro* culture) [24,28]. We found that the best performance was obtained with PLA/5MgTT, as the expression of the canonical osteogenic markers, RUNX2, SSP1, and BGLAP genes, Alkaline Phosphatase activity, type I Collagen, Osteopontin, Calcium deposits, and the lipids composition were more similar to that measured in stem cells induced to osteogenic differentiation by the culture in the osteogenic medium. Moreover, although the levels of the overall osteogenic markers were in a wide range among the PLA/5Mg-based composites cultures, they were consistently highest in PLA/5MgTT cell cultures (order PLA/MgTT > PLA/MgPEI > PLA/5Mg > PLA).

To our knowledge, for the first time, we found a remodeling of the lipid composition in the above hASCs on PLA/5Mg-based films. A lipidomic analysis by LC/MS QTOF mass spectrometry highlighted the reduction of fatty acids and the increase of selected phospholipids classes according to a previous report evaluating the fatty acid content in osteogenic differentiated mesenchymal stem cells [50]. Other works show changes in phospholipids content with osteogenic differentiation [51,53], and mainly with the increase of phosphatidylcholine, phosphatidylethanolamine, and phosphatidylinositol [50]. Of note, even compared to those publications, our data are novel since they referred to the lipidome remodeling in hASCs cultured on PLA/5Mg composite films.

We explained these results based on the capability of the PLA/5Mg, and mainly by PLA/5MgTT, to provide the cells the osteoinductive Mg, which is a cofactor of several enzymatic reactions necessary for the osteogenic differentiation, including those involved in the lipid biosynthesis and regulation [54–58]. The presence of released Mg by PLA/5Mg-based films was demonstrated in a co-culture trans-wells system, by which cells and films remained separated in the same culture chamber for 21 days in the growth culture medium. We found high levels of ALP expression in cell-PLA/5MgTT and to a lower extent in cell-PLA/5MgPEI and cell-PLA/5Mg co-cultures, whereas no ALP staining was observed in hASCs on neat PLA films.

These findings appear to contrast with earlier findings that showed a light expression of the osteogenic SPP1gene in the culture of hASCs on PLA. Indeed, this highlights the critical role of the synergistic effect of the PLA polymer film composition, the inclusion of Mg particles, and mainly the direct contact of the cells with the surface of the composites for inducing osteogenic differentiation.

Collectively, this work on the application of PLA and Mg-based composites in tissue engineering and regenerative medicine reveals a high potentiality of composite based on thermal-treated Mg particles, that it is on the right track to becoming the optimal 3D scaffold structure. Future works need to explore the suitability of the selected composite as 3D scaffold with defined porosity, pore dimension, shape and interconnectivity.

Supplementary data to this article can be found online at https://doi.org/10.1016/j.ijbiomac.2022.11.005.

CRediT authorship contribution statement

I.A., and S.M., conceived the research and designed the experiments. C.A, F.M., performed stem cell culture and polymer film experiments and analyzed data. F.D. performed polymer film production and characterization. I.T. performed gene expression experiments. R.M.P. performed Mass spectrometry analysis. F.M. performed computational lipidomic analysis. C.E., L.T., F.D., F.M., A.I, S.M. analyzed the data. C.A, I.A. and S.M, wrote the manuscript. A.F-M., M.L. and L.T. offered funds for the research. M.R. performed electron microscopy analysis. All authors read and approved the final version of the manuscript.

Declaration of competing interest

The authors declare the following financial interests/personal relationships which may be considered as potential competing interests: Luigi Torre, Marcela Lieblich reports financial support was provided by European Commission.

Acknowledgements

This work has been carried out within the M-ERANET Programme: Project POLYMAGIC.

A. Ferrandez-Montero thanks Project ADITIMAT-CM: Fabricación aditiva: del material a la aplicación. S2018/NMT-4411.

M. Lieblich thanks Project PID2019-104351GB-C21 financed by MCIN/AEI/10.13039/501100011033.

The authors thank Prof. U. Santamaria and Dott. G. Agresti, Laboratorio di diagnostica e Scienza dei materiali "Michele Cordaro", Tuscia University, for providing laboratory facilities.

References

[1] C. Argentati, F. Morena, I. Tortorella, M. Bazzucchi, S. Porcellati, C. Emiliani, S. Martino, Insight into mechanobiology: how stem cells feel mechanical forces and orchestrate biological functions, Int. J. Mol. Sci. 20 (2019) 5337, https://doi.org/10.3390/IJMS20215337, 20 (2019) 5337.

[2] F. Shang, Y. Yu, S. Liu, L. Ming, Y. Zhang, Z. Zhou, J. Zhao, Y. Jin, Advancing application of mesenchymal stem cell-based bone tissue regeneration, Bioact. Mater. 6 (2020) 666–683, https://doi.org/10.1016/J.BIOACTMAT.2020.08.014.

[3] C. Argentati, F. Morena, M. Bazzucchi, I. Armentano, C. Emiliani, S. Martino, Adipose stem cell translational applications: from bench-to-bedside, Int. J. Mol. Sci. 19 (2018), https://doi.org/10.3390/IJMS19113475.

[4] C. Argentati, I. Tortorella, M. Bazzucchi, F. Morena, S. Martino, Harnessing the potential of stem cells for disease modeling: progress and promises, J. Pers. Med. 10 (2020) 8, https://doi.org/10.3390/JPM10010008, 10 (2020) 8.

[5] I. Tortorella, C. Argentati, C. Emiliani, F. Morena, S. Martino, Biochemical pathways of cellular mechanosensing/mechanotransduction and their role in neurodegenerative diseases pathogenesis, Cells 11 (2022) 3093, https://doi.org/10.3390/CELLS11193093, 11 (2022) 3093.

[6] D. García-Bernal, M. García-Arranz, R.M. Yáñez, R. Hervás-Salcedo, A. Cortés, M. Fernández-García, M. Hernando-Rodríguez, Ó. Quintana-Bustamante, J. A. Bueren, D. García-Olmo, J.M. Moraleda, J.C. Segovia, A.G. Zapata, The current status of mesenchymal stromal cells: controversies, unresolved issues and some promising solutions to improve their therapeutic efficacy, Front. Cell Dev. Biol. 9 (2021), https://doi.org/10.3389/FCELL.2021.650664.

[7] M.Ben Abdeljawad, X. Carette, C. Argentati, S. Martino, M.F. Gonon, J. Odent, F. Morena, R. Mincheva, J.M. Raquez, Interfacial compatibilization into PLA/Mg composites for improved in vitro bioactivity and stem cell adhesion, Molecules 26 (2021), https://doi.org/10.3390/MOLECULES26195944.

[8] A. Ferrández-Montero, M. Lieblich, J.L. González-Carrasco, R. Benavente, V. Lorenzo, R. Detsch, A.R. Boccaccini, B. Ferrari, Development of biocompatible and fully bioabsorbable PLA/Mg films for tissue regeneration applications, Acta Biomater. 98 (2019) 114–124, https://doi.org/10.1016/J.ACTBIO.2019.05.026.

[9] W. Jahnen-Dechent, M. Ketteler, Magnesium basics, Clin. Kidney J. 5 (2012), https://doi.org/10.1093/NDTPLUS/SFR163.

[10] S. Yoshizawa, A. Brown, A. Barchowsky, C. Sfeir, Magnesium ion stimulation of bone marrow stromal cells enhances osteogenic activity, simulating the effect of magnesium alloy degradation, Acta Biomater. 10 (2014) 2834–2842, https://doi.org/10.1016/J.ACTBIO.2014.02.002.

[11] I. Groenendijk, M. van Delft, P. Versloot, L.J.C. van Loon, L.C.P.G.M. de Groot, Impact of magnesium on bone health in older adults: a systematic review and meta-analysis, Bone 154 (2022), 116233, https://doi.org/10.1016/J.BONE.2021.116233.

[12] J.H.F. de Baaij, J.G.J. Hoenderop, R.J.M. Bindels, Magnesium in man: implications for health and disease, Physiol. Rev. 95 (2015) 1–46, https://doi.org/10.1152/PHYSREV.00012.2014.

[13] O.A. Mederle, M. Balas, S.D. Ioanoviciu, C.V. Gurban, A. Tudor, C. Borza, Correlations between bone turnover markers, serum magnesium and bone mass

density in postmenopausal osteoporosis, Clin. Interv. Aging 13 (2018) 1383–1389, https://doi.org/10.2147/CIA.S170111.
[14] J. Liu, H. Zeng, P. Xiao, A. Yang, X. Situ, Y. Wang, X. Zhang, W. Li, W. Pan, Y. Wang, Sustained release of magnesium ions mediated by a dynamic mechanical hydrogel to enhance BMSC proliferation and differentiation, ACS Omega 5 (2020) 24477–24486, https://doi.org/10.1021/ACSOMEGA.0C02946.
[15] C. Zhao, H. Wu, J. Ni, S. Zhang, X. Zhang, Development of PLA/Mg composite for orthopedic implant: tunable degradation and enhanced mineralization, Compos. Sci. Technol. 147 (2017) 8–15, https://doi.org/10.1016/J.COMPSCITECH.2017.04.037.
[16] X. Li, W. Yu, L. Han, C. Chu, J. Bai, F. Xue, Degradation behaviors of mg alloy wires/PLA composite in the consistent and staged dynamic environments, Mater. Sci. Eng. C. 103 (2019), 109765, https://doi.org/10.1016/J.MSEC.2019.109765.
[17] G. Uppal, A. Thakur, A. Chauhan, S. Bala, Magnesium based implants for functional bone tissue regeneration – a review, J. Magnes. Alloy. 10 (2022) 356–386, https://doi.org/10.1016/J.JMA.2021.08.017.
[18] H. Cai, X. Li, C. Chu, F. Xue, C. Guo, Q. Dong, J. Bai, Insight into the effect of interface on the mechanical properties of Mg/PLA composite plates, Compos. Sci. Technol. 183 (2019), 107801, https://doi.org/10.1016/J.COMPSCITECH.2019.107801.
[19] R.A. Saari, M.S. Nasri, T. Kida, M. Yamaguchi, Impact of magnesium salt on the mechanical and thermal properties of Poly(vinyl alcohol), Polymers (Basel) 13 (2021), https://doi.org/10.3390/POLYM13213760.
[20] A. Ferrandez-Montero, M. Lieblich, R. Benavente, J.L. González-Carrasco, B. Ferrari, New approach to improve polymer-mg interface in biodegradable PLA/Mg composites through particle surface modification, Surf. Coat. Technol. 383 (2020), 125285, https://doi.org/10.1016/J.SURFCOAT.2019.125285.
[21] S.C. Cifuentes, M. Lieblich, F.A. López, R. Benavente, J.L. González-Carrasco, Effect of mg content on the thermal stability and mechanical behaviour of PLLA/Mg composites processed by hot extrusion, Mater. Sci. Eng. C. 72 (2017) 18–25, https://doi.org/10.1016/J.MSEC.2016.11.037.
[22] C. Argentati, F. Morena, P. Montanucci, M. Rallini, G. Basta, N. Calabrese, R. Calafiore, M. Cordellini, C. Emiliani, I. Armentano, S. Martino, Surface hydrophilicity of poly(l-lactide) acid polymer film changes the human adult adipose stem cell architecture, Polym 10 (2018) 140, https://doi.org/10.3390/POLYM10020140, 10 (2018) 140.
[23] F. D'Angelo, I. Armentano, S. Mattioli, L. Crispoltoni, R. Tiribuzi, G.G. Cerulli, C. A. Palmerini, J.M. Kenny, S. Martino, A. Orlacchio, Micropatterned hydrogenated amorphous carbon guides mesenchymal stem cells towards neuronal differentiation, Eur. Cell. Mater. 20 (2010) 231–244, https://doi.org/10.22203/ECM.V020A19.
[24] F. Morena, C. Argentati, E. Calzoni, M. Cordellini, C. Emiliani, F. D'Angelo, S. Martino, Ex-vivo tissues engineering modeling for reconstructive surgery using human adult adipose stem cells and polymeric nanostructured matrix, Nanomater. (Basel, Switzerland) 6 (2016), https://doi.org/10.3390/NANO6040057.
[25] C. Argentati, F. Morena, C. Fontana, I. Tortorella, C. Emiliani, L. Latterini, G. Zampini, S. Martino, Functionalized silica star-shaped nanoparticles and human mesenchymal stem cells: an in vitro model, Nanomater. (Basel, Switzerland) 11 (2021) 1–22, https://doi.org/10.3390/NANO11030779.
[26] F. Luzi, I. Tortorella, A.Di Michele, F. Dominici, C. Argentati, F. Morena, L. Torre, D. Puglia, S. Martino, Novel nanocomposite PLA films with lignin/zinc oxide hybrids: design, characterization, interaction with mesenchymal stem cells, Nanomater 10 (2020) 2176, https://doi.org/10.3390/NANO10112176, 20 (2019) 5337.
[27] L. Tarpani, F. Morena, M. Gambucci, G. Zampini, G. Massaro, C. Argentati, C. Emiliani, S. Martino, L. Latterini, The influence of modified silica nanomaterials on adult stem cell culture, Nanomater. (Basel, Switzerland) 6 (2016), https://doi.org/10.3390/NANO6060104.
[28] F. D'Angelo, I. Armentano, I. Cacciotti, R. Tiribuzi, M. Quattrocelli, C. Del Gaudio, E. Fortunati, E. Saino, A. Caraffa, G.G. Cerulli, L. Visai, J.M. Kenny, M. Sampaolesi, A. Bianco, S. Martino, A. Orlacchio, Tuning multi/pluri-potent stem cell fate by electrospun poly(l-lactic acid)-calcium-deficient hydroxyapatite nanocomposite mats, Biomacromolecules 13 (2012) 1350–1360, https://doi.org/10.1021/BM3000716/SUPPL_FILE/BM3000716_SI_001.PDF.
[29] S. Martino, F. D'Angelo, I. Armentano, R. Tiribuzi, M. Pennacchi, M. Dottori, S. Mattioli, A. Caraffa, G.G. Cerulli, J.M. Kenny, A. Orlacchio, Hydrogenated amorphous carbon nanopatterned film designs drive human bone marrow mesenchymal stem cell cytoskeleton architecture, Tissue Eng. Part A 15 (2009) 3139–3149, https://doi.org/10.1089/TEN.TEA.2008.0552.
[30] F. Morena, I. Armentano, P. Montanucci, C. Argentati, E. Fortunati, S. Montesano, I. Bicchi, T. Pescara, I. Pennoni, S. Mattioli, L. Torre, L. Latterini, C. Emiliani, G. Basta, R. Calafiore, J.M. Kenny, S. Martino, Design of a nanocomposite substrate inducing adult stem cell assembly and progression toward an epiblast-like or primitive endoderm-like phenotype via mechanotransduction, Biomaterials 144 (2017) 211–229, https://doi.org/10.1016/J.BIOMATERIALS.2017.08.015.
[31] R.M. Pellegrino, A. Di Veroli, A. Valeri, L. Goracci, G. Cruciani, LC/MS lipid profiling from human serum: a new method for global lipid extraction, Anal. Bioanal. Chem. 406 (2014) 7937–7948, https://doi.org/10.1007/S00216-014-8255-0.
[32] J.P. Koelmel, X. Li, S.M. Stow, M.J. Sartain, A. Murali, R. Kemperman, H. Tsugawa, M. Takahashi, V. Vasiliou, J.A. Bowden, R.A. Yost, T.J. Garrett, N. Kitagawa, Lipid annotator: towards accurate annotation in non-targeted liquid chromatography high-resolution tandem mass spectrometry (LC-HRMS/MS) lipidomics using a rapid and user-friendly software, Metab 10 (2020) 101, https://doi.org/10.3390/METABO10030101, 10 (2020) 101.
[33] H. Tsugawa, K. Ikeda, M. Takahashi, A. Satoh, Y. Mori, H. Uchino, N. Okahashi, Y. Yamada, I. Tada, P. Bonini, Y. Higashi, Y. Okazaki, Z. Zhou, Z.J. Zhu, J. Koelmel, T. Cajka, O. Fiehn, K. Saito, M. Arita, M. Arita, A lipidome atlas in MS-DIAL 4, Nat. Biotechnol. 3810 (38) (2020) 1159–1163, https://doi.org/10.1038/s41587-020-0531-2 (2020).
[34] G. Liebisch, E. Fahy, J. Aoki, E.A. Dennis, T. Durand, C.S. Ejsing, M. Fedorova, I. Feussner, W.J. Griffiths, H. Köfeler, A.H. Merrill, R.C. Murphy, V.B. O'Donnell, O. Oskolkova, S. Subramaniam, M.J.O. Wakelam, F. Spener, Update on LIPID MAPS classification, nomenclature, and shorthand notation for MS-derived lipid structures, J. Lipid Res. 61 (2020) 1539–1555, https://doi.org/10.1194/JLR.S120001025.
[35] R. Kurosawa, M. Takeuchi, J. Ryu, Fourier-transform infrared analysis of the dehydration mechanism of Mg(OH)2 and chemically modified Mg(OH)2, J. Phys. Chem. C 125 (2021) 5559–5571, https://doi.org/10.1021/ACS.JPCC.0C08696.
[36] B.V. L'vov, A.V. Novichikhin, A.O. Dyakov, Mechanism of thermal decomposition of magnesium hydroxide, Thermochim. Acta 315 (1998) 135–143, https://doi.org/10.1016/S0040-6031(97)00404-8.
[37] A. Kondo, R. Kurosawa, J. Ryu, M. Matsuoka, M. Takeuchi, Investigation on the mechanisms of Mg(OH)2Dehydration and MgO hydration by near-infrared spectroscopy, J. Phys. Chem. C 125 (2021) 10937–10947, https://doi.org/10.1021/ACS.JPCC.1C01470.
[38] Y. Chunmiao, Y. Lifu, L. Chang, L. Gang, Z. Shengjun, Thermal analysis of magnesium reactions with nitrogen/oxygen gas mixtures, J. Hazard. Mater. 260 (2013) 707–714, https://doi.org/10.1016/J.JHAZMAT.2013.06.047.
[39] A. Ferrández-Montero, M. Lieblich, R. Benavente, J.L. González-Carrasco, B. Ferrari, Study of the matrix-filler interface in PLA/Mg composites manufactured by material extrusion using a colloidal feedstock, Addit. Manuf. 33 (2020), 101142, https://doi.org/10.1016/J.ADDMA.2020.101142.
[40] T. Motoyama, T. Tsukegi, Y. Shirai, H. Nishida, T. Endo, Effects of MgO catalyst on depolymerization of poly-l-lactic acid to l, l-lactide, Polym. Degrad. Stab. 92 (2007) 1350–1358, https://doi.org/10.1016/J.POLYMDEGRADSTAB. 2007.03.014.
[41] I. Armentano, N. Bitinis, E. Fortunati, S. Mattioli, N. Rescignano, R. Verdejo, M. A. Lopez-Manchado, J.M. Kenny, Multifunctional nanostructured PLA materials for packaging and tissue engineering, Prog. Polym. Sci. 38 (2013) 1720–1747, https://doi.org/10.1016/J.PROGPOLYMSCI.2013.05.010.
[42] M.C. Fernández-Calderón, D. Romero-Guzmán, A. Ferrández-Montero, C. Pérez-Giraldo, J.L. González-Carrasco, M. Lieblich, R. Benavente, B. Ferrari, M. L. González-Martín, A.M. Gallardo-Moreno, Impact of PLA/Mg films degradation on surface physical properties and biofilm survival, Colloids Surf. B: Biointerfaces 185 (2020), 110617, https://doi.org/10.1016/J.COLSURFB.2019.110617.
[43] F. Morena, C. Argentati, M. Soccio, I. Bicchi, F. Luzi, L. Torre, A. Munari, C. Emiliani, M. Gigli, N. Lotti, I. Armentano, S. Martino, Unpatterned bioactive poly(butylene 1,4-cyclohexanedicarboxylate)-based film fast induced neuronal-like differentiation of human bone marrow-mesenchymal stem cells, Int. J. Mol. Sci. 21 (2020) 9274, https://doi.org/10.3390/IJMS21239274, 21 (2020) 9274.
[44] X. Zhang, Q. Chen, X. Mao, Magnesium enhances osteogenesis of BMSCs by tuning osteoimmunomodulation, Biomed. Res. Int. 2019 (2019), https://doi.org/10.1155/2019/7908205.
[45] T. Nakamura, A. Nakamura-Takahashi, M. Kasahara, A. Yamaguchi, T. Azuma, Tissue-nonspecific alkaline phosphatase promotes the osteogenic differentiation of osteoprogenitor cells, Biochem. Biophys. Res. Commun. 524 (2020) 702–709, https://doi.org/10.1016/J.BBRC.2020.01.136.
[46] X. Pang, K. Gong, X. Zhang, S. Wu, Y. Cui, B.Z. Qian, Osteopontin as a multifaceted driver of bone metastasis and drug resistance, Pharmacol. Res. 144 (2019) 235–244, https://doi.org/10.1016/J.PHRS.2019.04.030.
[47] L.A. Shiflett, L.A.M. Tiede-Lewis, Y. Xie, Y. Lu, E.C. Ray, S.L. Dallas, Collagen dynamics during the process of osteocyte embedding and mineralization, Front. Cell Dev. Biol. 7 (2019), https://doi.org/10.3389/FCELL.2019.00178/FULL.
[48] K. Uchihashi, S. Aoki, A. Matsunobu, S. Toda, Osteoblast migration into type I collagen gel and differentiation to osteocyte-like cells within a self-produced mineralized matrix: a novel system for analyzing differentiation from osteoblast to osteocyte, Bone 52 (2013) 102–110, https://doi.org/10.1016/J.BONE.2012.09.001.
[49] K.R. Levental, M.A. Surma, A.D. Skinkle, J.H. Lorent, Y. Zhou, C. Klose, J.T. Chang, J.F. Hancock, I. Levental, ω-3 polyunsaturated fatty acids direct differentiation of the membrane phenotype in mesenchymal stem cells to potentiate osteogenesis, Sci. Adv. 3 (2017), https://doi.org/10.1126/SCIADV.AAO1193.
[50] D.S.C. Bispo, L. Michálková, M. Correia, C.S.H. Jesus, I.F. Duarte, B.J. Goodfellow, M.B. Oliveira, J.F. Mano, A.M. Gil, Endo- and exometabolome crosstalk in mesenchymal stem cells undergoing osteogenic differentiation, Cells 11 (2022) 1257, https://doi.org/10.3390/CELLS11081257, 11 (2022) 1257.
[51] B. Teong, S.M. Kuo, C.H. Chen, Y.K. Chen, Z.J. Cheng, Characterization and human osteoblastic proliferation- and differentiation-stimulatory effects of phosphatidylcholine liposomes-encapsulated propranolol hydrochloride, Biomed. Mater. Eng. 24 (2014) 1875–1887, https://doi.org/10.3233/BME-140997.
[52] Y. Zhao, X. Chen, S. Li, R. Zeng, F. Zhang, Z. Wang, S. Guan, Corrosion resistance and drug release profile of gentamicin-loaded polyelectrolyte multilayers on magnesium alloys: effects of heat treatment, J. Colloid Interface Sci. 547 (2019) 309–317, https://doi.org/10.1016/J.JCIS.2019.04.017.
[53] L. Mao, M. Wang, Y. Li, Y. Liu, J. Wang, C. Xue, Eicosapentaenoic acid-containing phosphatidylcholine promotes osteogenesis:mechanism of up-regulating Runx2 and ERK-mediated phosphorylation of PPARγ at serine 112, J. Funct. Foods 52 (2019) 73–80, https://doi.org/10.1016/J.JFF.2018.10.027.
[54] V.P.S. Chauhan, S.S. Singh, A. Chauhan, H. Brockerhoff, Magnesium protects phosphatidylinositol-4,5-bisphosphate-mediated inactivation of casein kinase I in

erythrocyte membrane, Biochim. Biophys. Acta 1177 (1993) 318–321, https://doi.org/10.1016/0167-4889(93)90128-C.
[55] F. Gibellini, T.K. Smith, The Kennedy pathway—De novo synthesis of phosphatidylethanolamine and phosphatidylcholine, IUBMB Life 62 (2010) 414–428, https://doi.org/10.1002/IUB.337.
[56] N. Sasaki, M. Nobuo, K. Shirai, Y. Saito, A. Kumagai, Studies on CDP-choline:1,2-diacylglycerol cholinephosphotransferase activity in rat arterial wall, Atherosclerosis 43 (1982) 185–195, https://doi.org/10.1016/0021-9150(82)90021-1.
[57] M.D. Greenspan, J.M. Lowenstein, Effects of magnesium ions, adenosine triphosphate, palmitoylcarnitine, and palmitoyl coenzyme a on acetyl coenzyme a carboxylase, J. Biol. Chem. 243 (1968) 6273–6280, https://doi.org/10.1016/S0021-9258(18)94487-X.
[58] R.M. Scorpio, E.J. Masoro, Differences between manganese and magnesium ions with regard to fatty acid biosynthesis, acetyl-coenzyme a carboxylase activity and malonyl-coenzyme a decarboxylation, Biochem. J. 118 (1970) 391, https://doi.org/10.1042/BJ1180391.